

## REPORT DOCUMENTATION PAGE

AFRL-SR-AR-TR-07-0388

The public reporting burden for this collection of information is estimated to average 1 hour per response, including gathering and maintaining the data needed, and completing and reviewing the collection of information. Send comment information, including suggestions for reducing this burden, to Department of Defense, Washington Headquarters Serv 1215 Jefferson Davis Highway, Suite 1204, Arlington, VA 22202-4302. Respondents should be aware that notwithstanding any other provision of law, no person shall be subject to a civil or criminal penalty for failing to comply with a collection of information if it does not display a currently valid OMB control number.

**PLEASE DO NOT RETURN YOUR FORM TO THE ABOVE ADDRESS.**

1. REPORT DATE (DD-MM-YYYY) 9-25-2007	2. REPORT TYPE Final Performance Report	3. DATES COVERED (From - To) 7/1/2005-6/30/2007		
4. TITLE AND SUBTITLE UF Biomotor/Biosensor Nanotechnologies		5a. CONTRACT NUMBER		
		5b. GRANT NUMBER FA9550-04-1-0440		
		5c. PROGRAM ELEMENT NUMBER 0602712E		
6. AUTHOR(S) Richard B. Dickinson (PI), Daniel L. Purich (Co-PI), Gary McGuire (Co-PI), Brian Holliday (Co-PI), Denis Wirtz (Co-PI), William Cooke (Professor), William Zeile (Scientist), Suzanne Hens (Scientist), Kimberly Interlippi (Graduate Student), Colin Sturm (Graduate Student), Mellisa Thompson (Graduate Student).		5d. PROJECT NUMBER		
		5e. TASK NUMBER		
		5f. WORK UNIT NUMBER		
7. PERFORMING ORGANIZATION NAME(S) AND ADDRESS(ES) University of Florida Gainesville, FL 32611-6005 International Technology Center Research Triangle Park, NC 27709		8. PERFORMING ORGANIZATION REPORT NUMBER The College of William and Mary Williamsburg, VA 23187-8795 Johns Hopkins University Baltimore, MD 21218		
9. SPONSORING/MONITORING AGENCY NAME(S) AND ADDRESS(ES) Defense Sciences Office Defense Advanced Research Projects Agency 3701 N. Fairfax Drive Arlington, VA 22203		10. SPONSOR/MONITOR'S ACRONYM(S) Air Force Office of Scientific Research 875 North Randolph Street Arlington, Virginia 22203-1768		
		11. SPONSOR/MONITOR'S REPORT NUMBER(S)		
12. DISTRIBUTION/AVAILABILITY STATEMENT Figures 1-2 through 1-4 and 4-4 through 4-20 are from copyrighted publications. Approved for public release. Distribution unlimited.				
13. SUPPLEMENTARY NOTES n/a				
14. ABSTRACT This report contains a summary of activities on the project "UF Biomotor/Biosensor Nanotechnologies". Nanoscale actuators for use as molecular shuttles in biosensing devices were developed based on actin filament end-tracking motors. Novel strategies were developed exploiting these motors and modified substrata to propel and guide motor-coated micro- and nanoparticles using substratum-bound actin filaments with their elongating plus-ends bound to the particle surface. Key accomplishments of this project include (1) optimization of conditions for particle propulsion in cell extracts, (2) development of single-filament actuators, (3) guidance of single-filament elongation on patterned and microfabricated substrata, (4) development and validation of a mathematical model that predict particle propulsion velocity as a function of controllable parameters, (5) novel time-of-flight mass spectrometry methods to image surfaces, and (6) direct real-time methods to observe protein-protein interactions involved in filament end-tracking <i>in vivo</i> .				
15. SUBJECT TERMS Biomolecular Motors, Nanoscale Actuators, Actin Polymerization				
16. SECURITY CLASSIFICATION OF: a. REPORT U b. ABSTRACT U c. THIS PAGE U		17. LIMITATION OF ABSTRACT UU	18. NUMBER OF PAGES 52	19a. NAME OF RESPONSIBLE PERSON Richard B. Dickinson 19b. TELEPHONE NUMBER (Include area code) 352-392-0898

20071015193

---

## Final Report

---

**AFOSR #:** FA9550-04-1-0440

**TITLE:** UF BIOSENSOR/BIOMOTOR NANOTECHNOLOGIES

**Project Period:** 7/1/04-6/30/06 + 1 year extension to 6/30/07

**Lead Institution:** University of Florida  
**Sub-Award#1:** College of William & Mary  
**Sub-Award#2:** International Technologies Corporation  
**Sub-Award#3:** Johns Hopkins University

**PI:** Richard B. Dickinson, Professor  
Dept. of Chemical Engineering  
PO Box 116005, 221 CHE Bldg.  
University of Florida  
Gainesville, FL 32611-6005  
Tel: 352-392-0898 Fax: 352-392-9513 E-mail: dickinson@che.ufl.edu

**Co-PI:** Daniel L. Purich, Professor  
Dept. of Biochemistry & Molecular Biology  
PO BOX 100245  
University of Florida College of Medicine  
Gainesville, FL 32611-6005  
Tel: 352-392-1546 Fax: 352-392-1546 E-mail: dlpurich@ufl.edu

**Sub-Award #1 PI:** Brian Holloway, Associate Professor  
Department of Applied Science  
The College of William and Mary  
McGlothin-Street Hall, Room 305  
PO Box 8795  
Williamsburg, VA 23187-8795  
Tel: 757-221-3803; Fax: 757-221-2050 E-mail: holloway@AS.WM.EDU

**Sub-Award #2 PI:** Gary McGuire, PhD  
International Technology Center  
P.O. Box 13740  
Research Triangle Park, NC 27709  
Tel: 919-881-0500 Ext224 Fax: 919-881-0440 E-mail: gmcguire@itc-inc.org

**Sub-Award #4 PI:** Denis Wirtz, Professor  
Department of Chemical and Biomolecular Engineering  
Johns Hopkins University  
3400 N. Charles St.  
Baltimore, MD 21218  
Tel: (410) 516-7006 Fax: (410) 516-5510 E-mail: wirtz@jhu.edu

## A. Project Statement

A multidisciplinary team of biochemists and engineers, in a partnership between the University of Florida, William & Mary University (VA), Johns Hopkins University, and International Technology Centers (NC) has developed, and characterized actuators driven by nanoscale filament end-tracking motors. In living cells, end-tracking motors are responsible for

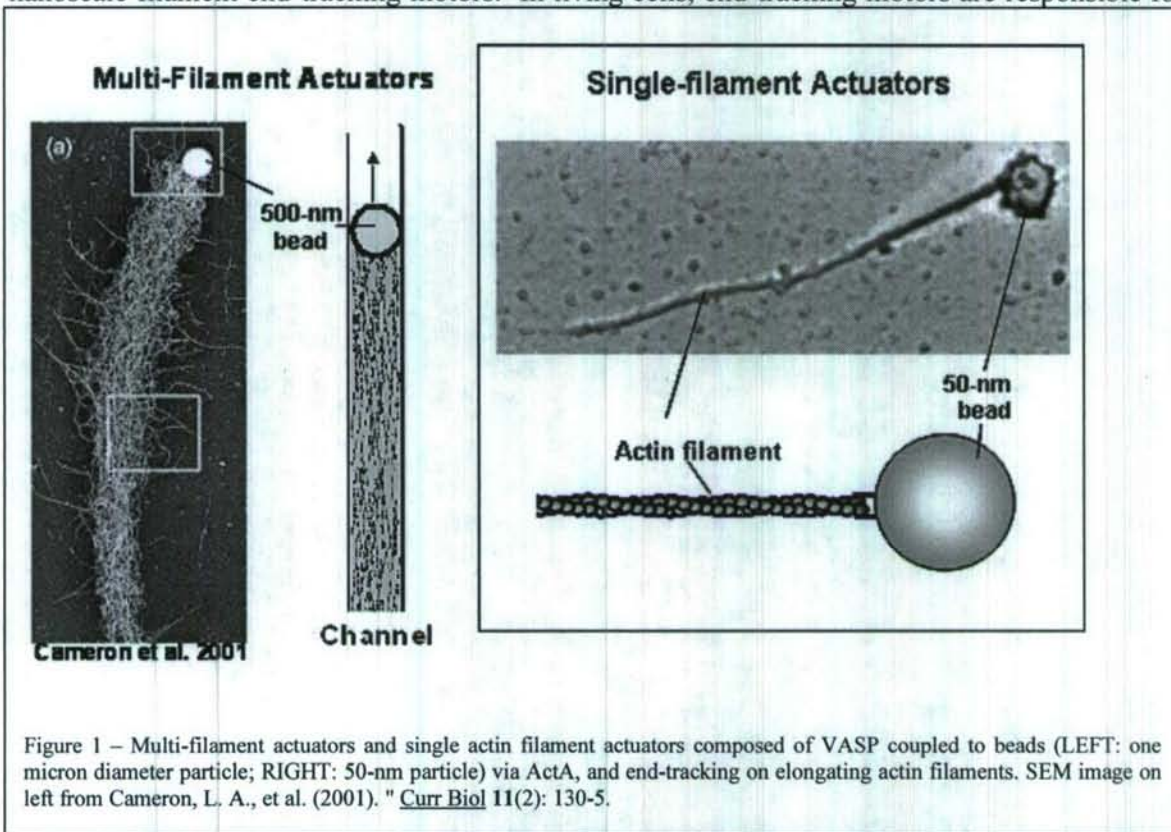


Figure 1 – Multi-filament actuators and single actin filament actuators composed of VASP coupled to beads (LEFT: one micron diameter particle; RIGHT: 50-nm particle) via ActA, and end-tracking on elongating actin filaments. SEM image on left from Cameron, L. A., et al. (2001). " Curr Biol **11**(2): 130-5.

cell-to-cell propulsion of invasive microorganisms by actin-based motility and for segregating daughter chromosomes during bacterial cell division. Filament end-tracking motors link one or several polymerization ends of protein filaments to a propelled object by binding strongly to elongating ATP-rich filament plus-ends. Single or multiple simultaneous interactions of end-tracking motors with polymerizing filament ends maintain the strong association between the stationary filaments and the propelled attached object (Figure 1). These special properties offer high potential for analogous function *in vitro* as nanoscale actuators of beads, spores, and DNA for transport and/or concentration of these species against diffusion gradients or opposing force fields. For example, filament-bound nanoparticles or protein complexes with attached oligonucleotides for hybridization may be used to target and separate specific DNA sequences without the need for a high-magnitude electric or magnetic field required for other separation technologies. Also, analogous to their function in actin-based motility of invasive organisms, end-tracking motors can also be used to improve separation and/or concentration of hazardous microorganisms for both better selectivity and improved detection limits. Fabricated micro- or

nano-channels and other surface modification or micro/nano-fabrication strategies are used to control the direction of propulsion and facilitate species separation. The project outcomes are to determine biochemical conditions and fabrication/surface modification strategies that may later be exploited for filament end-tracking actuation of bioagents in next-generation biosensing microdevices.

### **B. Vision Statement**

DARPA seeks novel strategies in the development of both rapid and unattended detection and identification systems of biowarfare agents with advantages over current multistep time-consuming and complex approaches. State-of-the-art approaches use antibody-based components with fluorescent reporters to detect the biowarfare agents and the Polymerase Chain Reaction (PCR) to amplify species-identifying DNA sequences. Success of this project will lead to novel strategies for detection and identification that do not rely on fluorescence or PCR. In addition to leading to novel designs of biosensing devices based on biomolecular motors, the proposal will enhance fundamental understanding of molecular motors as well as modify existing biomolecular machines and nanobiostructures for new functions. The broader technological impact of this work will be novel nano-scale actuators, which may lead to the future development of novel devices with potential applications in micro- and nano-fluidic systems. Such actuators are an entirely new concept in bionanotechnology. In addition, the scientific impact of this work will be a better fundamental understanding of these processes *in vitro*, as well as how living cells convert chemical energy into mechanical work during actin-based and microtubule-based cell motility in cell crawling and cell mitosis, which may lead to new therapeutic agents for combating invasive and metastatic cancers, gouty arthritis, Wiskott-Aldrich syndrome, as well as those neurodegenerative disorders linked to loss of functional synapses.

#### **Summary of Accomplishments:**

##### **Task-1: Biochemistry of filament end-tracking motors for propelling particles**

Daniel Purich (Task Leader), Richard Dickinson, William Zeile, Joseph Phillips, Colin Sturm, University of Florida

We have developed novel methods to propel ActA-coated particles propelled by single actin filaments (50-nm particles) and multiple filaments (0.5-mm particles). ActA is the surface protein of the intracellular pathogen *Listeria monocytogenes* that binds Vasodilator-Stimulated Phosphoprotein in order to hijack the host cell's actin polymerization system. ActA-coated particles in cell extracts likewise polymerize actin filaments, which propel the particle forward when the elongating filaments (or filament network) are bound and anchored to the substratum.

**Preparation of Protein Components and Motility Media** -- We have isolated and purified necessary proteins (rabbit skeletal muscle actin, prepared fluorescently-labeled actin and biotinylated actin), *Listeria* ActA protein (two forms), developed protocols for reliable preparation of cell-free extracts and prepared said extracts (bovine brain, rat brain, porcine brain, human platelet), and derivatized synthetic surfaces (glass microscope slides and cover glasses, fluorescent and non-fluorescent microspheres and quantum dots). We have designed flow cells and transfer cells and instructed in the use of these devices for microscopic observation. These

materials, agents and expertise have been used in Task 1: labeled muscle actin, ActA-NTA 0.5  $\mu$ m microspheres, ActA-CL 0.5  $\mu$ m microspheres, fluorescently labeled ActA and unlabeled ActA, cell-free extracts (rat brain), fixed *Listeria* bacteria competent for actin based motility. Activities in support of Tasks 2 and 4 include preparation of labeled and unlabeled muscle actin, ActA-CL 0.5, 0.2, and 0.05  $\mu$ m microspheres and quantum dots, cell-free extracts (human platelet), flow cell development and usage. Below are detailed protocols developed for the preparation of these materials and agents.

**Derivatization of polystyrene beads for binding His-tag fusion proteins** -- Suspension of amino polystyrene beads (500 nm) in 100 mM MOPS-KOH, pH 7.0, 10 mM ethylene glycobis-[succinimidylsuccinate] was added and incubated for 15 min at room temperature. 100 mM AB-NTA (N-[d-amino-1-carboxypentyl]-iminodiacetic acid) (Dojindo Laboratories) was added and incubated for 60 min. The beads are then washed four times with 100 mM MOPS-KOH and four times with 10 mM  $\text{NiCl}_2$  plus 10 mM glycine. Unbound  $\text{Ni}^{2+}$  was removed by washing four times with 100 mM MOPS-KOH. NTA microspheres were bound with ActA using purified ActA-His (see below).

**Derivatization of polystyrene beads for covalently linking ActA** -- A 0.5% suspension of Polysciences amino-modified 0.5 $\mu$ m microspheres (Cat# 07763) are prepared in 200  $\mu$ L MOPS Buffer (MB), (100 mM MOPS, pH 7.0). The microspheres are washed two times with MB by centrifugation at 14,000 rpm, 5 min, and 4C. BS<sup>3</sup> [Bis(sulfosuccinimidyl) suberate] crosslinker (Pierce) is added to beads for a final concentration of 2 mM and incubated at RT with shaking/mixing for 15 min. The microspheres are washed by centrifugation as before and resuspended in 200  $\mu$ L ActA protein solution (~250  $\mu$ g/mL) and incubated 1h, RT, with shaking/mixing. The microspheres are washed three times with 100 mM MOPS Buffer/100 mM glycine methyl ester, pH 7.0 and then washed one time with MB and resuspended in Brain Extract Buffer (BEB--20 mM Hepes-KOH, pH 7.4, 50 mM KCl, 2 mM  $\text{MgCl}_2$ , 5 mM EGTA, 1 mM EDTA, 100 mM sucrose)

**Derivatization of paramagnetic polystyrene beads for covalently linking ActA** -- A 0.5% suspension of Polysciences amino-modified 1-2  $\mu$ m paramagnetic particles (PMP) (Cat# 18879) are prepared using the same chemistry as for the microspheres for covalently linking ActA except that the centrifugation steps are replaced by magnetic separation.

**Preparation of *Listeria* ActA Proteins** -- *Listeria* ActA mutant expressing ActA-His (DP-L2723) or ActA-His-Cys (DP-L4363) (gifts of D.Portnoy) were cultured in Brain Heart Infusion media containing chloramphenicol (10  $\mu$ g/mL) for 8 hours at 37C. The bacteria were pelleted and protein was precipitated from the supernatant by adding ammonium sulfate to 50% saturation. Precipitated protein was resuspended in Hepes Binding buffer (HBB) (20 mM Hepes-KOH, pH 7.4, 50 mM KCl, 2 mM  $\text{MgCl}_2$ , 5 mM EGTA, 1 mM EDTA, 1 mM DTT) dialyzed overnight in same buffer and bound to a 5 mL BD TALON<sup>TM</sup> metal affinity resin column equilibrated in HBB. The column was washed with binding buffer and proteins were eluted with imidazole gradient (HBB plus 500 mM imidazole, pH 7.4). Eluted protein was further purified by Sephadex 75 (Pharmacia) gel-filtration chromatography. Protein was aliquoted, frozen, and stored at -80C.

## Preparation of rabbit skeletal muscle actin

### *Unlabeled Actin*

Acetone powder of rabbit skeletal muscle was prepared by the method of Spudich and Watt, 1971 and actin was purified from the powder by one cycle of polymerization and pelleting. The pellet was resuspended in G Buffer (2 mM Tris-HCl, pH 8.0, 0.2 mM ATP, 0.1 mM CaCl<sub>2</sub>, 0.5 mM DTT, 1 mM NaN<sub>3</sub>) and dialyzed against three changes of G buffer for 3 days. Concentration of unlabeled actin was measured by absorbance using an extinction coefficient of E<sub>290</sub>=26,000M<sup>-1</sup>cm<sup>-1</sup>.

### *Labeled Actin*

Monomeric actin (60 uM) was polymerized in polymerization buffer (2 mM MOPS pH 7.5, 50 mM KCl, 1 mM MgCl<sub>2</sub>, 0.2 mM ATP) for 4 hours. Fresh 10 mM stock solutions of Oregon green 488 succinimidyl ester and Alexa Fluor 488 succinimidyl ester (Molecular Probes, Eugene, OR) in DMSO were added to a 5 fold molar excess and incubated overnight with mixing at 4C. The next day the actin was centrifuged at 100,000 xg for 2h, the F actin pellet was resuspended in G buffer and dialyzed against two changes of G buffer over two days. The labeling efficiency was measured by using an extinction coefficient of E<sub>491</sub>=78, 000M<sup>-1</sup>cm<sup>-1</sup> for Oregon green and E<sub>491</sub>=76, 000M<sup>-1</sup>cm<sup>-1</sup> for Alexa Fluor 488. Labeling efficiency was greater than 70%.

### *Biotinylated Actin*

Biotin labeled actin was prepared by polymerization of monomeric actin in buffer without DTT. Actin Cysteine 373 was biotinylated by reacting the F actin with EZ-Link Maleimide-PEO<sub>2</sub> Biotin (Pierce, Rockford, IL) to a 5 fold molar excess and incubated overnight with mixing at 4C. The next day the actin was centrifuged at 100,000 xg for 2h, the F actin pellet was resuspended in G buffer and dialyzed against two changes of G buffer over two days. Moles of biotin per mole of actin was determined by the decrease in absorbance of avidin-HABA [2-(4'-hydroxyazobenzene) benzoic acid complex when biotin is added due to the higher affinity of biotin for avidin resulting in the displacement of HABA. By this method actin was labeled with 3 biotins per actin monomer.

## Motility Assays

### *Preparation of rat brain extract*

Frozen rat brain was pulverized and ground in liquid nitrogen, then mixed with an equal volume of Brain Extract Buffer (BEB) (20 mM HEPES (pH 7.7), 50 mM KCl, 2 mM magnesium chloride, 2 mM EGTA, 1 mM EDTA, 100 mM sucrose) supplemented with 0.5 mM ATP, 1mM leupeptin, 1 mM chymostatin, 1 mM pepstatin and 0.5 mM DTT as per (Yarar et al. 1999). The brain suspension was transferred to a glass homogenizer and ground for 20 passages on ice. A crude extract was prepared by centrifugation at 100,000 xg, 15 min, 4°C and frozen in liquid nitrogen for storage at -70 °C. A high speed supernatant was prepared by thawing and diluting the crude extract 10 times in BEB and centrifuging at 400,000 xg for 1 h, 4°C. The high speed supernatant was recovered concentrated to the original volume using a Centricon-10 micro-concentrator. The concentrated extract was adjusted to 200 mM sucrose, 7.5 mM acetate phosphate, 50 ug/mL acetate kinase, and 1 mM ATP. Aliquots were flash frozen in liquid nitrogen and stored at -70 °C. Protein concentration was 10 mg/mL by the Bio-Rad protein assay.

### *Preparation of human platelet extract*

Human platelet rich plasma was obtained from UF Blood Bank, units were pooled and erythrocytes removed by centrifugation at 160 xg, 20 min, RT. Platelets were washed three times in Platelet Wash Buffer (PWB) ( 20mM MES, pH 6.1, 50 mM KCl, 2 mM MgCl<sub>2</sub>, 10 mM EGTA, 10 mM EDTA, 0.5 mM ATP, 150 mM Sucrose) by centrifugation at 1000 xg, 20 min, RT, resuspended in sonication buffer (PWB plus 10 ug/mL leupeptin, 10 ug/mL pepstatin A, 10 ug/mL chymostatin, 1 mM PMSF and lysed by sonication. Sonicate was clarified by centrifugation at 100,000 xg, 1 h, 4C. Protein concentration of crude extract was 20 mg/mL by measuring absorbance at 280 nm.

**Coupling Motor Components to Particles** -- We have explored both covalent and non-covalent approaches to coupling *Listeria* ActA, which binds VASP from solution to form a complex, which together end-tracks polymerizing filaments. We found that nearly 100% of 500-nm beads being motile in platelet extracts could be achieved by the following protocol: ActA was expressed in *Listeria* and purified (Welch and Mitchison 1998) and was chemically cross-linked to 500 nm amino-modified beads with Bis(sulfosuccinimidyl) suberate or BS<sup>3</sup> (Pierce, Rockford, IL), a molecule containing N-hydroxysuccinimide groups on both ends (Zeile, unpublished). Crude platelet extract was made according to (Laurent et al. 1999). Complete platelet extract consisting of 75% (volume) crude brain extract, 10% creatine kinase adenosine tri-phosphate (ATP) regenerating solution (7.5mM creatine phosphate, 2 mM ATP, 2 mM Ethyleneglycol-bis(β-aminoethyl)-N,N,N',N'-tetraacetic Acid (EGTA), 2 mM MgCl<sub>2</sub>, 50 µg/mL creatine kinase), 10% protease inhibitors (10 µg/mL pepstatin-A, chymostatin, leupeptin, 1mM Phenylmethylsulfonyl Flouroide or PMSF), and 5% (10 mM) dithiothreitol (DTT) (Zeile et al. 2005). Actin tails formed on 500 nm beads from a solution containing 3.5 µM of Alexa 488-labeled Actin, ActA cross-linked 500 nm beads, and complete platelet extract, containing among many other proteins, approximately 7 µM of actin. The actin tails were observed in both phase contrast and fluorescence.

**Analysis of Motor Function** -- Consistent with optimizing the functionality of surface-bound motor components, we have explored how the phosphorylation state of VASP regulates its activity in the propulsion of particles. The understanding how these actin motors can be turned on and off also has critical importance for our efforts to construct a biosensor/biomotor device. There is great precedent in the literature for this idea. VASP is phosphorylated on three critical residues (serine 153, serine 235, and threonine 274, murine VASP numbering) and VASP phosphorylation regulates actin binding, actin filament bundling, and actin nucleating activity (Harbeck et al. 2000; Horstrup et al. 1994; Lambrechts et al. 2000). The affinity of VASP for its tethering molecule (ActA in the case of *Listeria*, zyxin and vinculin in the case of membrane associated cytoskeletal anchors) is controlled by the phosphorylation state of VASP and the goal of this on-going project is to reveal this mechanism.

To understand the on/off mechanism of the ActA/VASP actin motor we have prepared paramagnetic particles (1-2 um) with covalently bound *Listeria* ActA. ActA-derivatized paramagnetic particles (ActA-PMP) will be used in separation experiments to isolate key components of the ActA/VASP actin motor. We are interested in isolating VASP in the state in which VASP is most competent for actin-based motility. In addition, we are interested in discovering ancillary motor proteins that may be isolated by this method. The paramagnetic

particles have been tested for the ability to support actin motility in human platelet cell-free extracts

To investigate the preferred phosphorylation state of VASP in the actin-based motility of the ActA/VASP actin motor, we applied the ActA-PMP to cell-free extracts of human platelets under conditions that would mimic conditions for motor assembly and that would allow isolation of motor complexes when separated from the bulk extract solution. In Figure 1-1, Lane 1, are seen the two forms of VASP in extract before the ActA-PMP are applied. VASP phosphorylated on serine 153 is seen as the band migrating at 50 kDa and the dephosphorylated form is the band at 46 kDa. During incubation of ActA-PMP with extract, motor complexes are formed on the ActA-PMP. Once formed, the ActA-PMP are extensively washed and motor complexes are eluted with increasing salt. Dephosphorylated VASP is eluted at 200 -300 mM KCl, Lane 7 and 8, with some VASP eluting at 500 mM KCl, indicating a high affinity of VASP for ActA. This preliminary experiment forms the first evidence that ActA/VASP actin motor complexes may form preferentially with the dephosphorylated form of VASP. If this result can be believed, it is then possible that turning off the actin motor may only require introduction of a protein kinase and/or activation of a protein kinase. The high affinity of VASP for ActA-PMP observed in these experiments also further confirms our observation of microsphere and *Listeria* actin-based motility in which motor complexes form tight associations with their major component

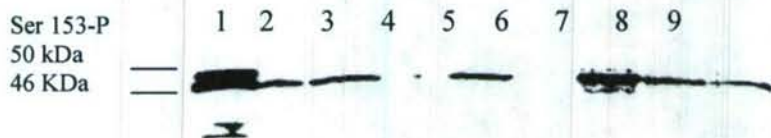


**Figure 1-1:** ActA-PMP selectively binds the dephosphorylated form of VASP in platelet extracts. Human platelet extracts were incubated with ActA covalently linked paramagnetic particles (ActA-PMP) for 30 min at room temperature under low salt buffer conditions. The particles were washed extensively until the absorbance returned to baseline. Motor complexes were eluted with a KCl step gradient. Proteins were TCA precipitated and loaded on SDS-PAGE gels for transfer to membrane for Western analysis. The membrane was probed with Anti-VASP monoclonal antibody (BD Biosciences). Lane 1, platelet extract before treatment with ActA-PMP indicating the two forms of VASP present (dephospho-VASP, 46 kDa, phospho-VASP, 50 kDa). Lane 2, fraction containing unbound proteins. Lane 3-6 wash fractions. Lane 7, Fraction eluted with 200 mM KCl. Lane 8, Fraction eluted with 300 mM KCl. Lane 9, Fraction eluted with 500 mM KCl.

**Development of Single-Filament Actuators --** We have shown that by optimizing bead size and biochemical conditions, we can observe single actin filament plus-ends binding to the surface of a bead under an electron microscopy (EM). ActA was covalently bound to the bead surface allowing for a much stronger surface to protein bond. Beads were bound to the glass surface to prevent wash out of sample during EM treatment. Silica beads were used for a stronger covalent bond to ActA (silanation) and a reliable method to purify beads from excess ActA and bind beads to a glass substrate (silica density is greater than polystyrene).

#### *Functionalized 50 nm Beads for use in Motility Assay*

A 95% ethanol solution was prepared and the pH adjusted to 4.5 to 5.5 using acetic acid ( $\text{CH}_3\text{COOH}$ ). Two percent 3-aminopropyltriethoxysilane (APES) in 95% ethanol solution was prepared and mixed for 15 minutes. Beads (Polysciences cat#24040 stock is at 5.63% (v/v)) were then diluted 10x with 95% ethanol. Beads were washed two times with 95% ethanol and

pulse sonicated between washes (30 pulses at 20% level 1 power). The beads were then aspirated and the APES solution was added and mixed for 3 minutes. The functionalized beads were washed two times with 95% ethanol and pulse sonicated between washes (30 pulses at 20% level 1 power). The supernatant was removed and beads allowed to cure overnight at room temperature in humidity <60% (alternative is to heat to 100°C for 30-60 minutes to cure). Beads were then resuspended in H<sub>2</sub>O and pulse sonicated (30 pulses at 20% on level 1 power) and stored at 4°C.

#### *ActA and BSA Conjugate to 50 nm Beads*

The beads surface was activated with 0.2% glutaraldehyde and incubated at room temperature for 30 minutes while shaking. The beads were then washed in BEB and pulse sonicated (30 pulses at 20% level 1 power). The amount of protein to add to the beads was determined by first calculating the surface area of beads by taking the product of the volume of stock beads and surface area of one bead by the volume of one bead (0.338 m<sup>2</sup> for 50 μL of 5.63% (v/v) stock beads). The mass/area of ActA (0.905 mg/m<sup>2</sup>) was then determined by taking the molecular weight of ActA (68,000 g/mol for ActA and 66,000 g/mol for BSA) divided by the circumference of the Stokes radius of ActA (6.3 nm for ActA and 3.5 nm for BSA). The product of bead area and protein mass/area resulted in the theoretical amount of protein to coat the beads. Protein was added to the beads and incubated for 45 minutes at room temperature while shaking. The beads were then washed in BEB (the supernatant was saved to test the amount of protein not bound) and pulse sonicated. If beads were to be fluorescently labeled, the fluorescent BSA was calculated and conjugated to the bead at this point. Beads were then washed 2 times in 100 mM glycine methyl ester in BEB and pulse sonicated between washes. Beads were washed once more in BEB and stored at 4°C.

#### *Flow Chamber for Exchange Experiments*

Flow chambers were made using parafilm or double sided tape arranged in two parallel lines as support for a cover slip on top of a microscope slide. A pipette was used to introduce material to the flow chamber while filter paper was used to extract the fluid creating the flow. To bind nanospheres or *Listeria* in the flow chamber, the cover slip was first treated with APES and glutaraldehyde (vesicles will adsorb to the glass surface and no glass treatment is necessary). Three-aminopropyltriethoxysilane treated cover slips were made by exposing clean cover slips to a 2% APES in 95% ethanol solution (APES solution was mixed for 15 minutes prior) for 2 minutes. Cover slips were then washed in a porcelain tray 2 times with 95% ethanol in a beaker. Excess liquid was removed and cover slips incubated overnight at room temperature unsealed for curing (humidity <60%).

#### *Substratum-bound particles*

An APES cover slip was charged with 2% glutaraldehyde for 20 minutes at room temperature. The cover slip was washed with water, a flow chamber prepared, and diluted ActA beads/*Listeria* was flowed through (an appropriate bead/*Listeria* cover slip surface coverage was determined by testing different dilutions) and incubated at room temperature for 20 minutes. Excess binding sites were quenched with BEB containing 100 mM GME for 20 minutes. The chamber was washed with BEB and a motility assay was added for the desired amount of polymerization time.

### *Preparation for Electron Microscopy*

Two percent glutaraldehyde in 0.1 M sodium cacodylate buffer was added to the flow chamber for 20 minutes. A 0.1% tannic acid was then added for 20 minutes and rinsed with 3 exchanges of water. Uranyl acetate (UA) at 0.2% was added for 20 minutes. The entire slide was submerged in water and the cover slip removed. A metal cage with lens paper at the bottom was submerged in the water and the cover slip was placed inside the cage sample side up (never exposed to air). Several samples were stacked in the cage separated by lens paper (including lens paper to cover the top cover slip). The cage containing samples was transferred to a 10% ethanol solution and incubated with mixing for 5 minutes. The cage was then transferred to 20%, 40%, 60%, 80%, and 2 times in 100% for 5 minutes each, then 0.2% UA in 100% ethanol for 20 minutes, and finally 2 times in molecular sieved 100% ethanol for 5 minutes each (Svitkina and Borisy 1999). At this point the samples were optionally placed at 4°C overnight.

The critical point dryer was filled with molecular sieved 100% ethanol and the cage containing the samples was placed in the CPD and sealed. Liquid CO<sub>2</sub> was added until all ethanol was removed from the chamber. The temperature and pressure was increased to the critical point of CO<sub>2</sub>. CO<sub>2</sub> gas was removed until completely evacuated. The sample was removed and either coated for SEM or TEM or placed in a desiccator until coating was done.

The cover slip with sample was placed on a 13 mm SEM stub using double sided tape to affix (sample side up). The sample was then placed in the sputter coated and filled with argon gas. The pressure was then reduced and the sample was sputter coated with gold palladium at 45 milliamps for 30 seconds. The sample was then imaged using SEM.

Samples were placed in a rotary shadower at an angle of 45° for platinum coating. The chamber was evacuated and the sample was coated with carbon platinum with a setting of 2.1 kV and 60 mA. Samples were coated with a 5 nm thickness of platinum which was monitored using a quartz thickness monitor. The sample angle was adjusted to 90° for carbon coating with a setting of 1.9 kV and 90 mA. The sample was coated for 8 seconds resulting in approximately a 5 nm coating of carbon (to strengthen sample).

A razor blade was used to cut 0.5 mm<sup>2</sup> sections from edge to edge across the entire surface of the metal coated sample. Areas that did not contain sample were colored with a black marker. The cover slip (sample side up) was floated on 10% hydrofluoric acid (HF) until the glass cover slip sinks (about 15 minutes). A platinum loop was used to transfer the floating pieces to water. Again the platinum loop was used to transfer pieces to a 100% solution of bleach (6.13% sodium hypochlorite [NaOCl]) and incubated for one hour. Pieces were transferred to water and then placed on polyvinyl formal coated 200 mesh TEM grids. Grid containing samples were dried overnight at room temperature and later viewed with TEM with a voltage of 75 kV.

Polyvinyl formal coated copper 200 mesh grids were used as support for samples in TEM imaging. To coat grids with polyvinyl formal, formvar (0.25% to 0.4% (w/v)) was mixed with chloroform in a glass container large enough for a microscope slide to be submersed. A glass microscope slide was cleaned using 70% ethanol dried with a Kim wipe. The slide was coated with a household cleaning solution and polished with lens paper to prevent the plastic from sticking strongly to the glass surface when trying to separate in water. The glass slide was dipped into the polyvinyl formal and allowed to incubate for a few seconds. The slide was then removed at a constant velocity to give a smooth uniform coating. The faster the slide is removed the thicker the film will be on the slide. Thicker layers were formed by dipping the slide several times (allowing the chloroform to evaporate between dips). A sharp metal edge was used (such as the edge of tweezers or a razor blade) to scrape the edges of the glass slide and to cut across

the middle of the slide so the film will separate. At approximately a 30° to 45° angle to the water the slide was slowly submersed causing the film to separate from the slide and float away. Grids were placed on the film (rough side up, shiny side down) avoiding any discontinuities in the film and avoiding film edges. A note card or parafilm cut to the size of the film was placed on top and in a sweeping motion the card was dunked and rotated up to pull the grids and film out of the water on top of the card or parafilm which was then dried for 24 hours.

**Results** – To test motility conditions, 500-nm polystyrene beads were first attached to a glass surface and exposed to a motility assay. The biomimetic particles produced actin rocket tails similar to the *Listeria* rocket tails (Figure 1-2). These large particles produced too many filaments to observe single filament interactions with the surface. The number of filaments was reduced by reducing the bead size from 500 nm to 200 nm which produced beads with fewer filaments but still too many to give conclusive evidence of filament attachment. The particles were reduced again from 200 nm to 50 nm which resulted in only a few filaments associated with each beads.

Filament density was also controlled by adjusting the ActA surface density, the extract concentration, and the actin polymerization incubation time. At optimal ActA density for observing single filaments corresponded to approximately 13 ActA proteins per bead. The extract was used at full strength and actin concentrations in the range of 3 to 5  $\mu\text{M}$  produced single actin filaments quickly (less than one minute) (Figure 1-3 and 1-4).

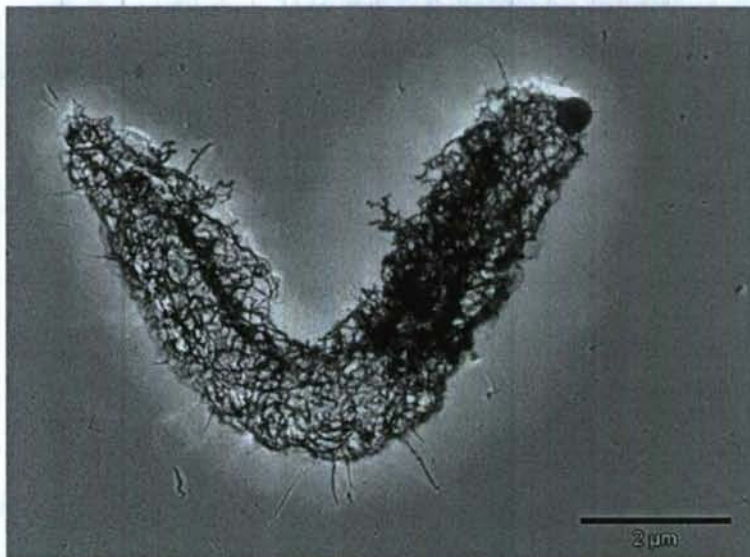


Figure 1-2. A 500 nm polystyrene nanosphere with an actin rocket tail viewed using TEM. From (Sturm 2007).

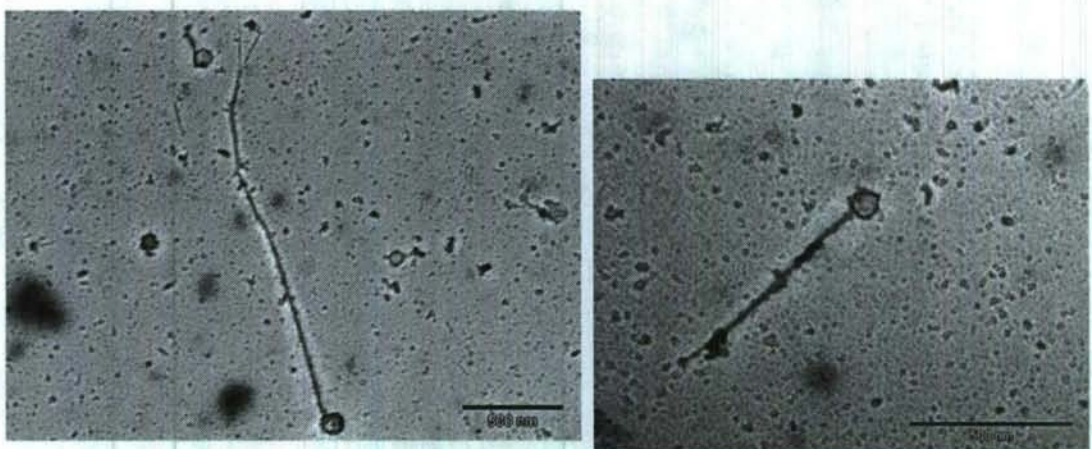


Figure 1-3 Examples of actin filaments elongating by insertional polymerization from 50 nm silica beads. From (Sturm 2007).

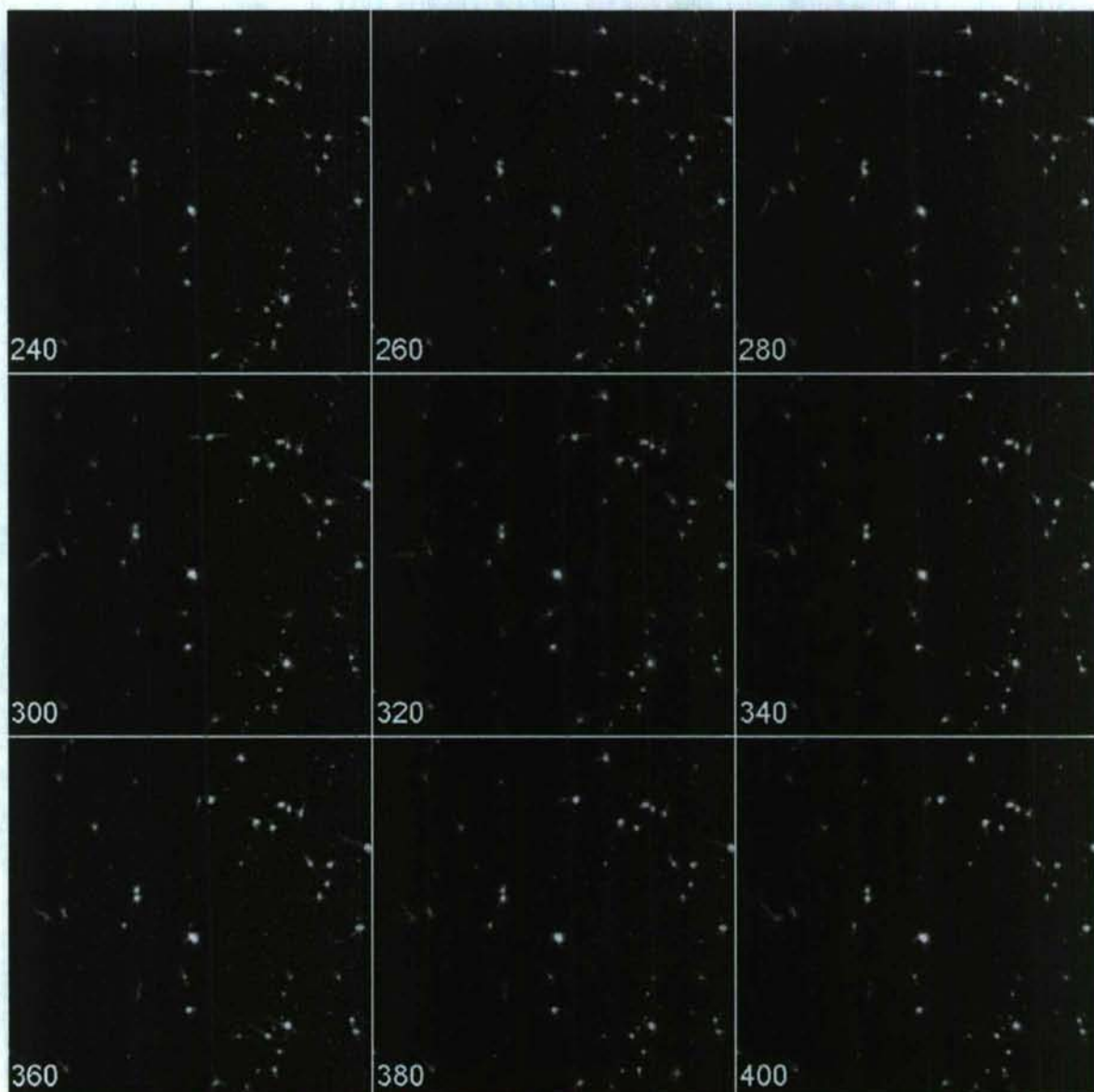


Figure 1-4. Time lapse of single actin filaments emanating from 50 nm beads. Beads are labeled with rhodamine and actin is labeled with Oregon-green. Motility assay started and focused after 4 minutes. Images taken at 20 second intervals. From (Sturm 2007).

## Task 2: Substratum Modification for Guidance of Propelled Particles

Suzanne Hens, Gary McGuire, Mark Ray, Darin Thomas, International Technologies Center (ITC)

ITC has provided surfaces and microchannel architectures for the study of biomotor activity of actin filaments. Although much of the proposed work included substratum modification, we limited the fabrication of substrata to those that had a square cross-section. We expect that square channels are more favorable than other substrata architectures, such as the proposed sterically hindered "V" design. Nanostructured surfaces were produced using glass substrates. Since glass does not have a mirrored surface, as does silicon, photolithography on these substrates produces an undercut in the photoresist. In the case of microtubule biomotors, the undercut is necessary to retain the biomotor within the channel. The effect of undercutting microchannels on actin filament processivity has not been previously evaluated. In addition to the tasks outlined in the original proposal, ITC completed the following additional tasks:

- 1) Provided and evaluated PDMS stamping methods for myosin on glass substrates. This work led to a paper submitted by R. Dickinson to Langmuir.
- 2) Demonstrated the capability patterning myosin by the MIMIC (micromolding in capillary) method.
- 3) Designed and demonstrated the capability of PDMS stamping alkylsilanes for patterning on planar surfaces.
- 4) Fabricated PDMS microfluidic channels for direct delivery of biomotors to substrates.
- 5) Developed biomotor channels in Cytop, which inhibits protein binding.

Biomotor propulsion is dependent upon microchannel width, depth, surface shape and surface chemistry, thus a systematic study of these contributions is required. Using a planar surface with microchannel surface patterning allows for the effect of only the microchannel width, and thus providing simplest design architecture. Perhaps one of the simplest methods for patterning planar surfaces with binding and nonbinding regions is to use PDMS printing methods, including micromolding in capillaries (MIMIC).

### ***PDMS Stamping***

A PDMS stamping protocol was designed for myosin printing on glass, such that the myosin tracks were activated for protein binding, whereas the adjacent surfaces were passivated with nonbinding regions. Although PDMS stamping allows for micron-sized control of protein binding structures, MIMIC is advantageous for its alignment control of protein channel patterns. Since the MIMIC stamp can be reoriented before wicking the protein solution, MIMIC is more useful when alignment is necessary.

Myosin was patterned with PDMS stamps using a similar protocol for stamping self-assembled monolayers, see Figure 2-1. The protein solution was incubated on the hydrophobic PDMS surface for 1 hour at room temperature. The protein solution was then removed from the surface and the stamp was dried with compressed dry air flow, after which the stamp was pressed against an unmodified glass surface and allowed to incubate at room temperature for 60 minutes under a weight. The stamp was removed and the glass surface was dried with compressed air.

In addition to printing proteins, we were able to stamp aminosilane onto a silicon

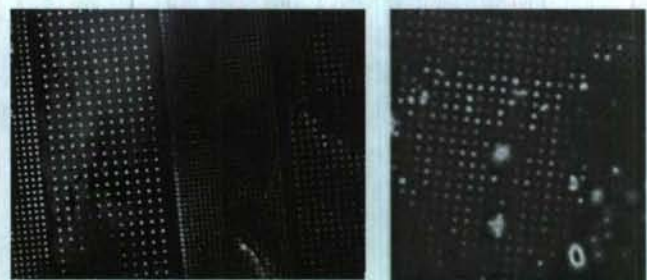


Figure 2-1. Microscopic images of PDMS stamped glass surfaces patterned with IgG-FITC antibody (left) and myosin protein (right).

oxide surface with high precision (see Figure 2-2). These amino tracks can then be modified by conjugate chemistries that bind actin filaments. The protocol used for this process followed the self-assembled monolayer stamping methods used for stamping alkanethiols on gold.

In order to confirm that the amino silane was stamped and that the amine group is sterically accessible for coupling reactions, we treated this amine group with our nanodiamond fluorophore probes. Nanodiamonds (NDs) are advantageous as fluorophore probes since they exhibit fluorescence emission at many excitation wavelengths and are resistant to photobleaching. Furthermore, polydispersed samples are visible under the microscope. For this work, we coupled the aminosilane patterned surface to ozonated nanodiamond using EDC coupling reagent, Sulfo-NHS additive in MES buffer. Ozonated nanodiamond has a carboxylic acid surface functional group that links to an amine to form an amide bond. After the coupling reaction was completed, the



Figure 2-2. Microscopy photos of PDMS stamping of APES on  $\text{SiO}_2$  surfaces. All features are less than 10 microns in size.

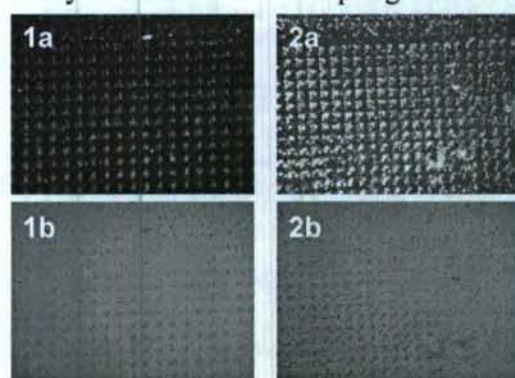


Figure 2-3. Confirmation of reactive amino groups from microcontact stamping APES. After ND coupling reaction (2) and control (1), the substrate was imaged in dark field (a) and bright field (b).

slides were sonicated three times and rinsed with acetone. Thus, the APES patterned surface showed a brighter image for the ND reaction compared with the control reaction without nanodiamond, see Figure 2-3. This experiment confirmed that our stamping protocol was sufficient to produce surface functional amines for protein conjugation.

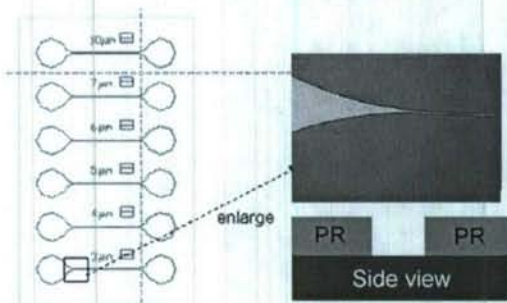


Figure 2-4. Confirmation of reactive amino groups from microcontact stamping APES. After ND coupling reaction (2) and control (1), the substrate was imaged in dark field (a) and bright field (b).

its ability to guide actin filaments. Instead of silicon, glass microchannels were fabricated for its ease of visualization of fluorescent tags by microscopy. We designed biomotor mask #1 with microchannels having dimensions 10, 7, 6, 5, 4, 3 microns wide, see Figure 2-4. In addition to channel size, channel depth was also varied, with 2 microns being the smallest depth.

#### **PDMS Microfluidic Channels**

Mask #1 also provided a means of designing microfluidic cells with channels of 3, 5, and 50 microns wide. Microfluidic cells were fabricated in PDMS by molding against a silicon wafer patterned with photoresist (see Figure 2-5) and sealing the PDMS microchannels with a glass slide. These samples allow for ease of delivery of actin

motors directly to the channel and can be visualized directly on the microscope stage. Using microfluidics simplifies the study of actin binding by directly delivering the protein to the desired site. Control of the biomotor delivery along the microchannel is also possible with this device.

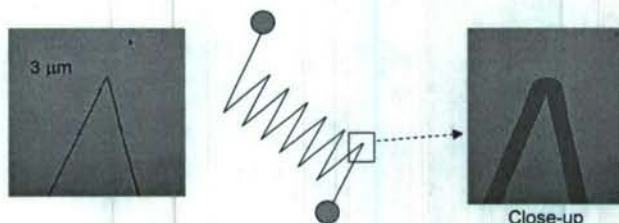
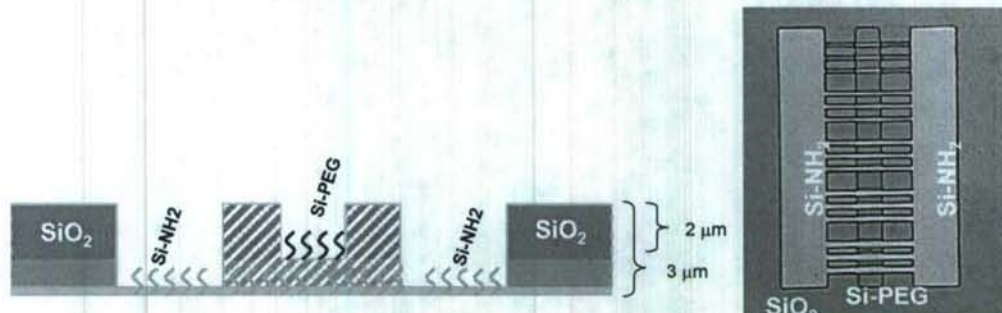


Figure 2-5. Microfluidic AutoCAD drawing shown with photographs of the photoresist pattern on silicon.

#### **Silicon Substrates**

For the third level of guidance complexity, we fabricated a three chamber architecture design in silicon with protein binding microchannels and protein nonbinding surfaces from biomotor mask design #2 (see Figure 2-6). This design allows for simultaneous comparative analysis of the dimensional affect on the propulsion of guided biomotors. Since the distance between channels was small, microscopic monitoring of multiple channels was possible. Fabrication of this design relied on traditional microelectronic processing and produced a three-level structure, allowing the biomotors to migrate from a protein passivating chamber to the microchannel, which binds protein.

After the biomotor moves down the length of the microchannel, it dumps into an outer chamber that inhibits protein binding and thus propulsion. With different microchannels widths in close proximity, video microscopy can be used to compare the effect of this parameter on biomotor assembly and processivity.



**Figure 2-6.** Schematic drawing of the cross-section for the three chamber design. The microchannel cross-section is in the foreground (surface modified with aminosilane) and the inner chamber is in the background (surface modified with silane-polyethyleneglycol). Upper right corner: Microscopic photograph (100x) of the device in silicon.

The three chamber system on silicon was difficult to use on an inverted fluorescence microscope. Also it was determined that the fluorescence emission of the photoresist was undesirable since the biomotor fluorophores were also red. Furthermore, the chips were difficult to handle due to their small size and did not allow for active movement of buffer solutions through their capillary action method. Although this structure should have been ideal, we changed the substrate to glass to provide an easier platform for microscopic visualization and coupling of the excitation light.

#### *Glass Substrates*

In addition to the fabrication of silicon platforms for biomotor traction, we fabricated platforms on microscope glass coverslips that allow for ease of visualization and coupling of fluorescence light for total internal reflection. We attempted to make channels within glass coverslips by wet etching glass that was photopatterned. This method was not successful due to the formation of uneven channel edges.

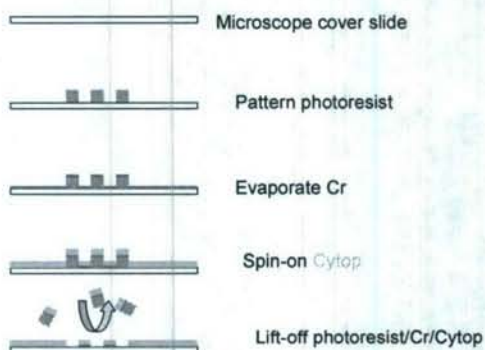


Figure 2-7. Processing sequence for Cytop patterned channels.

It was found in the literature that the fluoropolymer, similar to Teflon called Cytop, which is hydrophobic and does not bind proteins, may be patterned on glass coverslips leaving channels that have glass platforms, see Fig 2-7. This glass platform can be modified with APES to provide amine surface groups for protein attachment.

The formation of Cytop channels follows typical microfabrication processing methods, see Figure 2-7. First the cover slide

is photopatterned with two coatings of a negative photoresist (NFR016) that has a retrograde profile, which facilitates lift-off processing. Next, a chrome layer is made on the glass slide using an e-beam evaporator that coats only the top surfaces of the glass and photoresist material, leaving the photoresist sides uncoated to facilitate lift-off. Chrome serves as an adhesion layer for Cytop (Lee et al. 2005) and at 50 Å it is transparent for microscopy. Cytop is spin-coated onto the glass slide at 4,000 rpm for 20 sec and is cured on a hot plate at 100 °C for 10 minutes. The appearance of Cytop can be seen as a colorful film over the entire slide. Next, the slide is soaked in acetone for 5 minutes and then sonicated briefly at low power to facilitate lift-off. The depth of the channels and the surface uniformity of Cytop are then measured using our Alpha-Step IQ profilometer. The glass channels can be surface modified with amines by incubating the substrate in 10% APES in ethanol (anhydrous) for 60 minutes; APES in toluene was found to degrade Cytop. We observed fluorescence emission from incubation of FITC-streptavidin after coupling sulfo-NHS-biotin to the amine surface groups with EDC.

In this work, we patterned a series of lines of different thicknesses and densities to study the mechanism of biomotor processivity. The thickness of the Cytop layer used is dependent upon the photopatterned feature size and resolution, since the polymer layer must be thinner than the photoresist for lift-off. For example, in Figure 2-8 Cytop was patterned around 5 and 20 micron thick lines. For the highest density of lines (Density 3), the 20 micron features were resolved but the 5 micron features did not. The thickness of Cytop for this slide was ~ 2 microns, which is about the minimum thickness required to study 500 nm actin-coated beads. Larger feature patterns allow for thicker photoresist and ultimately a thicker Cytop layer. In this case, the Cytop layer did not have a flat profile; the profile showed a marked increase in height at the edges of the channel, as if the polymer was pulled along the photoresist by capillary action. This type of profile does not allow for good sealing of the polymer on the glass slide, forming an inadequate channel. It is possible that dilution of Cytop, along with successive layering to achieve the desired thickness, may mitigate this effect.

The patterning for Mask #3 was found insufficient for the experimental set-up used by our collaborators for the study of the biomotors. In their set-up, they created a flow cell by wicking the biomotor buffer solution across a microscope coverslip that was much larger (18 mm x 18 mm) than the channel sizes used. In addition, it was difficult to study the biomotor processivity for such short channels. Furthermore, a reservoir would be useful to supply large quantities of biomotor to the channel. Thus, an additional design was requested, shown in Figure 2-9 (not to scale). For this design the channel thicknesses are still on the order of 4 to 20 microns wide, but the channels span the length of the coverslip. A similar design was used in the biomotor Mask #1 design that had similar

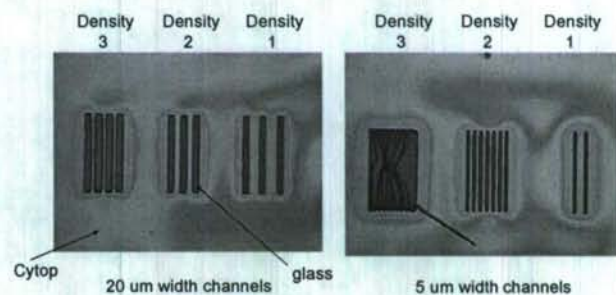


Figure 2-8. Cytop patterned channels from Mask #3 design showing the success of patterning is dependent upon the density of lines.

channel widths, but were  $\sim 10$  mm long. Thus, we used this mask design to trouble-shoot any fabrication issues prior to making a separate mask.

The biomotor mask #1 has channel widths as small as 3 microns thick and as large as 10 microns thick. However, in this case, since these thin lines are relatively long it was difficult to perform lift-off after curing Cytop on the glass slide. In analogy, the lift-off process for such features can be thought of as pulling a microscopically thin piece of spaghetti out of a channel. We found that the lift-off was incomplete, especially for the smaller feature widths. Thus, it was suggested that a series of reservoirs could be placed along the channel width to shorten their length and still provide a reservoir for chemical/biochemical biomotor supplies.

It was uncertain if this mixture of feature sizes that were several orders in range would be feasible to fabricate; lift-off for features that are hundreds of microns in size is also difficult. However, our process engineer suggested using a common method that includes physical lift-off prior to chemical lift off. Physical lift-off is done by using tape to remove the metallic layer that has poor adhesion to photoresist surfaces. For this work, we found that physical lift-off was successful. We found that physical lift-off requires a gold coating on chrome. After physical lift-off was complete, we removed the gold layer using a gold wet etch solution that contains potassium iodide and does not affect the photoresist. After the gold layer was removed, we then soaked the substrate in acetone to facilitate chemical lift off. For the best results, we found that it is important to complete the entire process in one day.

We used Mask #1 for testing the formation of Cytop channels in a pattern that has both large and small features; in this case, we used the ladder structures, see Fig 2-4 above. Two glass slides were made that had open channel reservoirs that were connected by 10 and 8 micron wide channels. We were unsuccessful in resolving smaller channel widths due to the thickness of the photoresist. The larger reservoir features were resolved, whereas the smaller ladder features were mostly unsuccessful. For the smaller ladders, it appeared that the photoresist was removed along the channel length, but the Cytop remained forming a tunnel. Our profilometer showed that the Cytop layer was less than a micron thick, which is the lower limit of channel depth. These substrates were sent to our collaborators for testing. We made a mask design, see Fig 2-10, which is used for testing the reservoir and channel widths. Eight mask designs will fit on a four inch wafer.

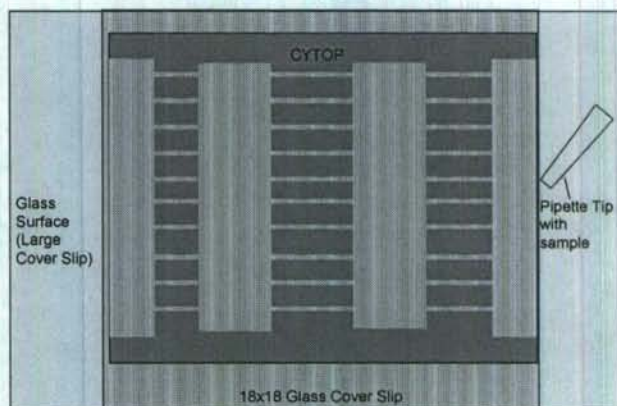


Fig. 2-9. Concept drawing of the experimental set-up that shows the desired channel and reservoir architecture in Cytop (not drawn to scale).

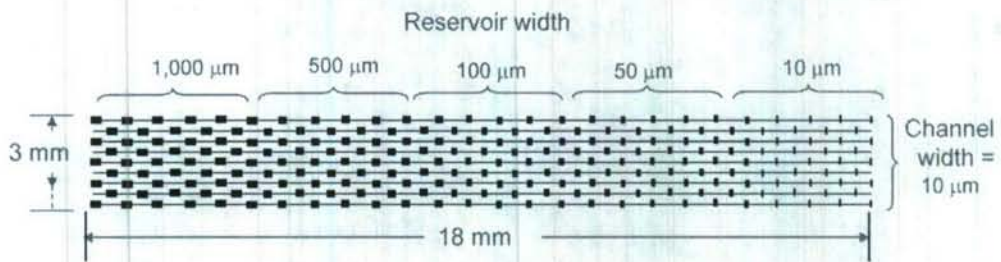


Fig. 2-10. Design for mask #4 consisting of continuous channels of different widths (10  $\mu\text{m}$  shown) and rectangular reservoirs of different sizes contained within an  $18 \times 18 \text{ mm}^2$  area.

### *Surface Chemical Characterization*

ITC independently tested the surface functionalization protocol for rendering the surface with amines and PEG groups from their respective silane. For this analysis we cleaned silicon substrates with pirhana for 10 min., rinsed with water 3x, sonicated in water 10 min, dried substrates under  $\text{N}_2$ , and placed in a toluene solution containing either Si-PEG or Si-NH<sub>2</sub>. Modifications of silicon with PEG and NH<sub>2</sub>, as well as glass modification with PEG were completed. The XPS data for PEG modification on silicon showed a fragmentation pattern with peaks at 288 eV (C-O) and 284 eV (C-C-C), as well as a small peak for Si-C near 288 eV. The silicon slide that was treated with APES showed a two peaks overlapping at ~284 eV, corresponding to similar energies for breaking the two C-C bonds of the alkane chain between Si and NH<sub>2</sub>. These results provide strong evidence of successful surface functionalization.

### Task 3 - Composition/Topological Characterization

Brian Holliday (Task Leader), William Cooke, College of William & Mary

Our primary task has been to support the biomotors device development via the characterization of the surfaces of the devices, especially with respect to the location and identification of biological molecules of interest to the project. Time-Of-Flight Secondary Ion Mass Spectrometry (TOF-SIMS) is our primary method for obtaining high resolution images of surfaces differentiated by their molecular construction. TOF-SIMS focuses a high energy (5-10 keV) primary ion of gold, or gold clusters, onto a surface, and then determine the mass to charge ratio of the ejected particles by measuring their speed following acceleration through an electrical potential (typically 7 kV). The high primary energy enables tight focusing, to construct high resolution images. TOF-SIMS is not traditionally considered an effective tool for imaging biomolecules because the high energy of the primary ion impact routinely fragments any massive biomolecules as it ejects and ionizes them. Although we have not characterized any biomotors devices during this project, we have made significant strides in detecting and imaging biomolecules by developing an automated peak-picking method that also automatically aligns separate spectra to enhance their resolution. We have also developed automated Region Of Interest (ROI) detectors that sifts through the myriad of spectral lines to determine which ones best characterize physical structures. Finally, as a result of our software enhanced resolution techniques, we have been able to use an unbunched primary ion beam, which significantly improves our spatial resolution. Each of these advances are described in more detail below.

By using gold cluster ion beams, we have detected peptides as heavy as 1200-1500 Da. In Figure 3-1, we show an image of a droplet, constructed by filtering only on the parent ion of angiotensin. The concentric rings result from concentration gradients formed as the solution droplet evaporates. These rings are complementary to similar structures formed when this same data is imaged using  $\text{Na}^+$  ions. However, the low level of the signal from the small number of parent ion counts limits the resolution and the contrast of the image. Almost always, there is far more signal in the low mass region, and fragmentation of the vasopressin produces some of this signal. The difficulty, of course, is identifying which parts of this spectrum are due to fragmentation of the vasopressin. Things will necessarily become far more difficult when multiple species of biomolecules are simultaneously present, in overlapping patterns.



**Figure 3-1:** TOF-SIMS image formed by filtering on the mass of angiotensins. This rectangle is 200 microns on a side.

To address this problem, we have developed a high throughput technology designed to quickly and completely analyze the multitude of ion masses that are usually present in TOF-SIM spectra of biological samples. There are two key concepts for this procedure: (1) dimension reduction to decrease the number of bits of information present in any TOF-SIMS spectrum to the minimum possible, and (2) mass-resolution enhancement, to increase the density of the minimal pieces of information.

To accomplish the first task, we have developed an automated peak-picking algorithm that quickly locates the position of mass-spectrum lines, and assigns them an amplitude. In a typical spectrum, there are 2-3 million detected events. Our automated peak-picker uses a filter-like process to determine the maximum likelihood for the location and amplitude of a single ionic isotope, modeling the Poisson noise inherent in any counting detector. The net result is that the automated peak-picker reduces a typical spectrum from 600,000 time steps to only 315 lines, as shown in Figure 3-2. This peak-picker also locates the peaks with a remarkable precision, often much better than 1 part in 100 of the nominal line width of a feature. The peak-picker does miss some small peaks – mostly those with a peak count of less than 40 events. However, these peaks only account for less than  $10^{-6}$  of the total signal.

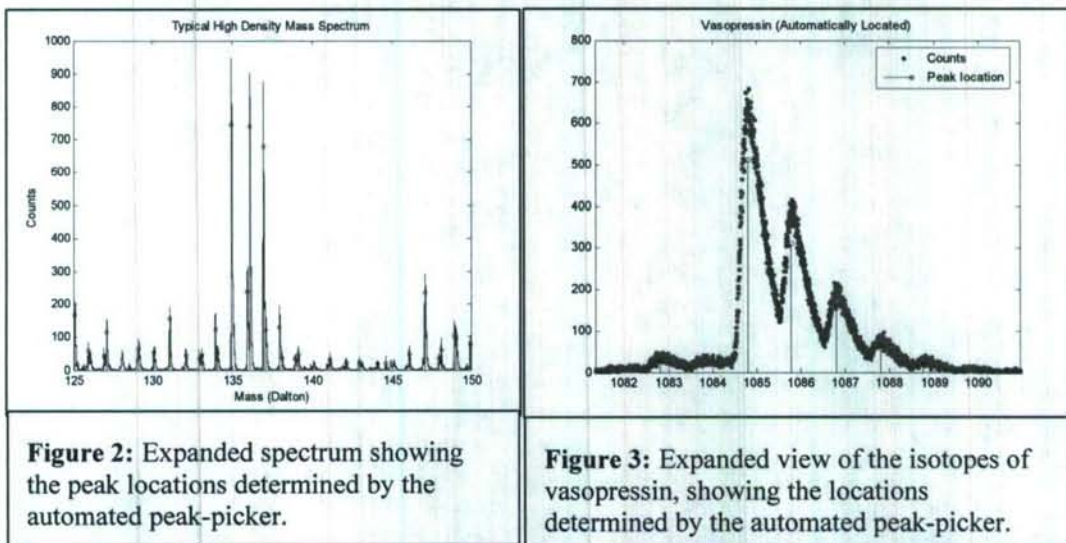
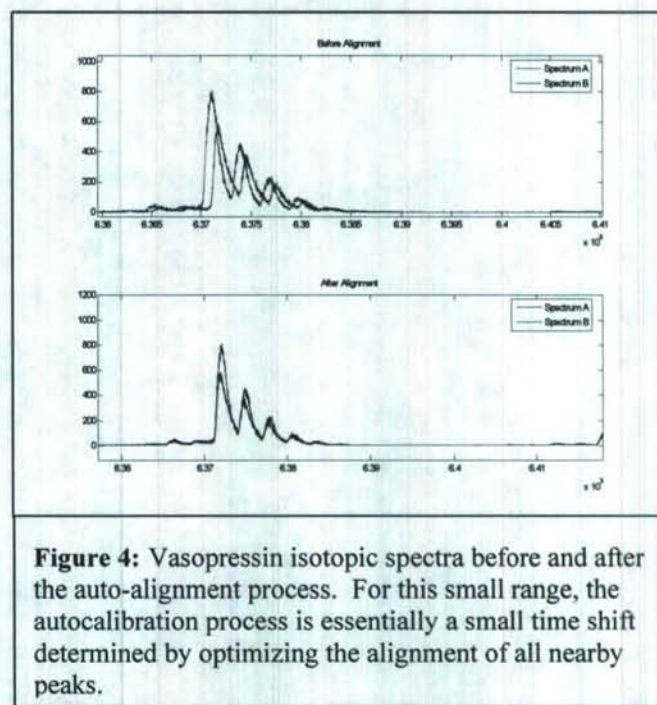


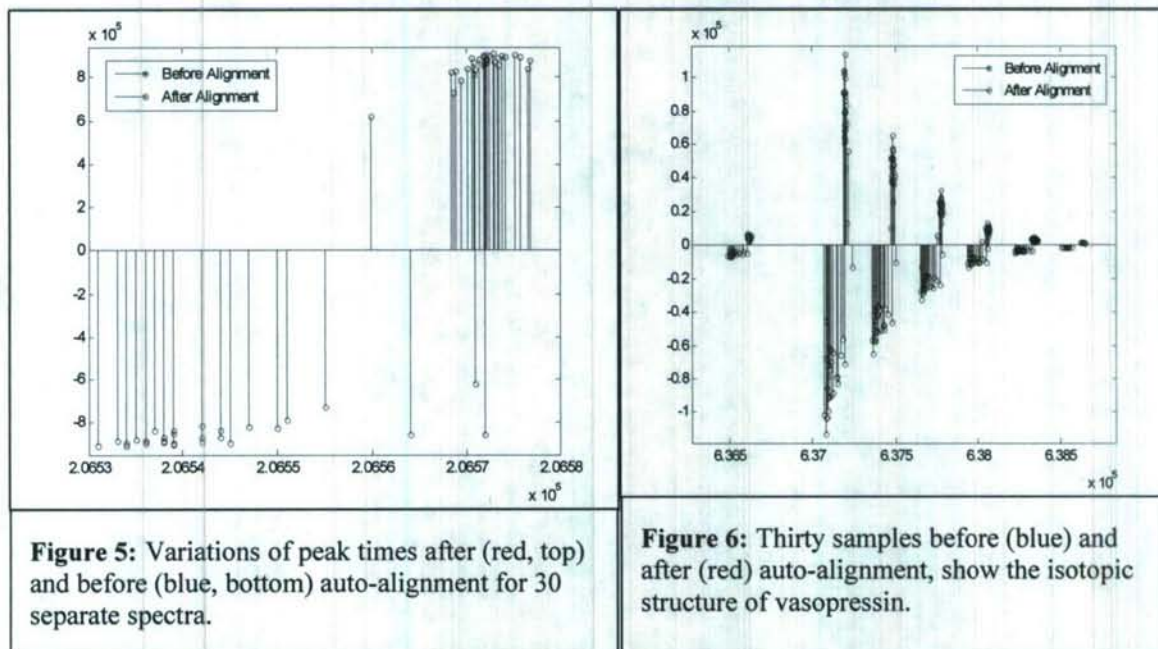
Figure 3-3 shows a more expanded view of the spectrum near the isotopes of vasopressin, along with the peak positions found by the automated peak-picker. This automated process actually determines peak position much better than is evident in Figure 3-3. To demonstrate this, we have used the automated peak picker to find all the peaks in 30 separate samples of vasopressin deposited on silver foils. For each sample, we used the automated peak-picker to find peaks, and then developed an automated alignment process that corrects for time offsets, and small acceleration voltage fluctuations by optimizing the match among all the peaks shared by at least two spectra. This means that we are typically adjusting the same two parameters adjusted during a TOF-SIMS calibration, but instead of matching two known ions, we are matching all the detected lines, without needing to know what ions those lines represent.

Figure 3-4 shows some typical results for two of the 30 spectra, before and after the auto-alignment process. This auto-alignment process weights all peaks equivalently, although a future version will give greater emphasis to the larger peaks, which inherently have higher precision. Nevertheless, this current version aligns peaks to have less than 10 time steps of variation from one sample to the next, over the entire spectrum.

For a silver ion, one of the largest signals for anything deposited on a silver foil, 10 time steps mean a mass precision of 1 part in  $10^4$ , as shown in Figure 3-8. This mass is not accurate to this level, but rather it is merely repeatable to 1 part in  $10^4$ . As this measurement is not an attempt to determine a mass value, but rather an attempt to identify if two peaks represent the same



**Figure 4:** Vasopressin isotopic spectra before and after the auto-alignment process. For this small range, the autocalibration process is essentially a small time shift determined by optimizing the alignment of all nearby peaks.



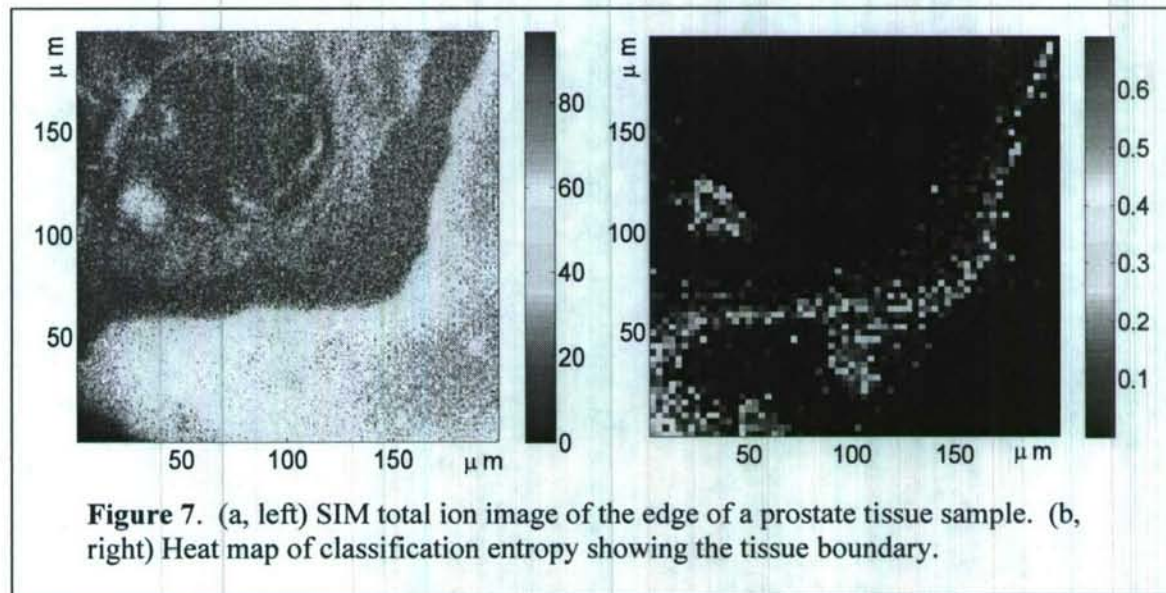
**Figure 5:** Variations of peak times after (red, top) and before (blue, bottom) auto-alignment for 30 separate spectra.

**Figure 6:** Thirty samples before (blue) and after (red) auto-alignment, show the isotopic structure of vasopressin.

ion, this high precision is entirely sufficient.

This high precision of 10 time steps of scatter in the values of the automated peak-picker following auto-alignment persist even to very high masses. In Figure 3-6, the autoalignment process, which is based on all the detected peaks, reduces the scatter from a value of nearly half the 1 Da splitting between isotopes by almost an order of magnitude. This enhanced resolution makes it possible to filter on specific isotopes to create better resolution images. Figure 3-6 shows how the enhanced resolution produced by the automated peak-picker and autoalignment procedure

With the improved resolution provided by the automatic peak-picking and alignment, we found that it is now possible to image structures using the molecular signatures of the many fragment ions produced by ion-impact on the parent molecule. This plethora of information implies a new challenge: automatically identifying which patterns represent real physical structures, versus random apparent patterns. As an example, we have examined slices of prostate tissue and kidney tissue, where the low mass restriction of SIMS makes it virtually impossible to see any parent biological ions. Figure 3-7 show SIMS prostate tissue imaging, along with our automatic detection of Regions Of Interest (ROI). On the left hand side, we show a total-ion signal collected from a thin slice of prostate tissue that had been embedded in a polymer (OCT) before cutting. Both the polymer (the high count region at the bottom) and the tissue are visible. The tissue region contains perhaps 40 cells, although this total ion image provides very little information about cell boundaries, and nothing about structures smaller than a cell. However, each of the 256X256 pixels in this image contains an entire mass spectrum, while the total ion signal is simply the sum of the counts in each of these pixels. We have applied our biomarker discovery software tools to construct a classifier that distinguishes between the tissue region and the polymer based on the pattern of signal amplitudes using only five of the many hundreds of mass peaks. The right hand figure shows the boundary these tools constructed, using the Shannon entropy calculated from the probability estimates that our classifier provides of a particular pixel being tissue or polymer. This figure does not show the actual classifier results, which clearly marks the tissue region as



tissue and the polymer region as polymer. This simply illustrates that our tools can automatically divide hyper-spectral SIMS images into distinct structures with clear boundaries.

There is an inherent trade-off in SIMS imaging between high mass resolution and high spatial resolution. For the highest mass resolution, bunched incident ions produce as short a timing pulse as possible, but space charge limitations limit the spatial resolution of the ion focusing. However, with our improved peak-picking and automatic alignment, we find we can reduce the mass resolution, while still maintaining excellent discrimination between isotopic peaks – sufficient to separate isotopic structure at  $m/z \sim 1000$ . Hence, we use a primary ion beam that is *not* bunched to improve our spatial resolution. Figure 3-8

shows the image of a kidney cell using a (high mass resolution) bunched beam, while Figure 3-9 shows the same cell using an unbunched beam. The very small channels in the cell wall show real structure that is evident in several different runs taken after moving the sample to insure that the narrow feature do not represent imperfections in the ion focusing optics. The smallest visible structures in the image with the unfocussed beam are approximately 1-2 microns. These structures are also evident in images constructed from filtered signals, using, for example, only sodium ions.

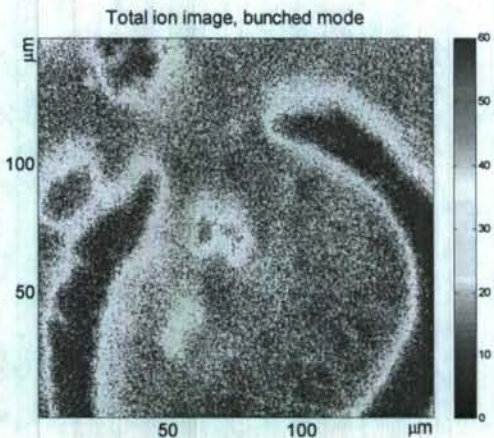


**Figure 8:** Kidney cell total ion image using bunched (high mass resolution) primary ion beam.

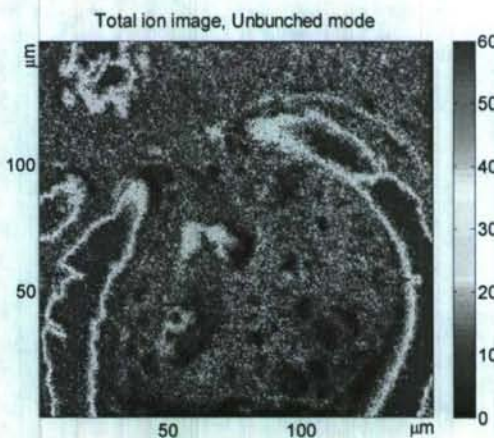


**Figure 9:** Kidney cell total ion image using an unbunched primary ion beam (low mass resolution).

#### **Task 4 – Biophysical Modeling and Characterization**

Richard B. Dickinson (Task Leader), Daniel Purich, Kimberly Interliggi, Colin Sturm, Joseph Phillips, William Zeile, University of Florida

**Microscopy-Based Tracking Methods for Measuring Velocities** - The performance of the biomotors for propelling particles is being assessed using microscopy-based tools, brought online in the last twelve months. Total Internal Reflection Fluorescence Microscopy (TIRFM), which images only fluorophores within ~100 nm of the surface, is used to directly observe and analyze the elongation and substratum-binding of individual actin filaments. Normal fluorescence microscopy is used for low-resolution tracking of larger particles, and a laser-tracking system has been assembled and is operational for high-resolution particle tracking. This latter technique also incorporates a gradient-optical trap for force-velocity measurements. However, our primary focus has been on velocity measurements and other characterizations of motility in different conditions using simultaneous measurement of multiple particles, which required only low resolution methods.

**Characterization of Motility on NEM-Myosin-Coated Surfaces** -- To attach actin filaments and tails to glass surfaces, we used an inactivated form of the F-actin-binding protein, myosin (Cytoskeleton, Denver, CO). Modification with N-ethylmaleimide (NEM) irreversibly inactivates the catalytic site of myosin (Amann and Pollard 2001; Kuhn and Pollard 2005). The protocol modified from Kuhn and Pollard (Kuhn and Pollard 2005) was used to inactivate myosin with N-ethylmaleimide and to adsorb the molecules onto a cleaned glass surface. Lyophilized myosin (Cytoskeleton, Inc., Denver, CO) was resuspended in 200  $\mu$ L of 10 mM PIPES (1,4-Piperasinediethanesulfonic acid) buffer, pH 7.0, and 0.8 M KCl for a final concentration of 10  $\mu$ M myosin. The myosin was treated with 1-mM NEM for 1 hour on ice and then 1 mM DTT for 1 hour on ice to sequester any unreacted NEM. The myosin was dialyzed using gel filtration spin columns (Pierce) against a solution of myosin dialysis buffer (10 mM Imidazole pH 7, 0.5M KCl, and 10mM ethylenediaminetetraacetic acid (EDTA) and 1mM DTT) to filter unreacted NEM and DTT complexes from the solution. The final myosin solution was placed -20° C freezer in 50% glycerol. The concentration of the NEM-myosin was tested by an absorbance assay. Myosin extinction coefficient,  $b$ , is known to be 0.53cm<sup>2</sup>/mg at 280nm. Based on the measured absorbance,  $A$ , the concentration,  $c$ , of NEM-myosin is calculated by Beer's Law ( $A=\epsilon bc$ ). Using this inactivation method, the final concentration of myosin was on average 2.85±0.04  $\mu$ M.

NEM-myosin is diluted in the myosin dialysis buffer to 0.1  $\mu$ M or 1  $\mu$ M and pipetted into a flow chamber containing a clean glass cover slip surface for ten minutes. The surface is then washed with a Bovine Serum Albumin (BSA) solution in myosin dialysis buffer at 1% w/v. This passivates the parts of the glass surface that do not contain myosin, decreasing non-specific interactions of the actin filament tails to the glass surface. The BSA is removed after approximately five minutes and the sample to be tested is flowed into the chamber (Kuhn and Pollard 2005).

To confirm the presence of myosin on the surface of the glass, we probed the surface with stabilized actin filaments. Unlabeled actin monomers were allowed to

polymerize in solution for five minutes, followed by addition of Rhodamine-labeled phalloidin was then added to the solution. Phalloidin is a peptide that specifically binds and stabilizes actin filaments, preventing them from depolymerizing. The stabilized filaments were then allowed to flow into the flow chambers and incubated for five minutes. The flow chambers were washed one time with buffer and then sealed. Figure 4-1 shows the TIRF images from this experiment, which confirmed the presence of inactivated myosin on the surface. These images are showing only 200 nm into the sample, suggesting that any filaments seen are attached to the surface. The BSA surface (control) shows no filaments present, while the 1- $\mu$ M NEM-myosin treated surface contained actin filaments that were visible in TIRF, even after a wash to remove all unattached filaments. The filaments on the myosin treated surface fluctuated very little, indicating they were attached more strongly on the myosin, while the few filaments on the BSA-treated control were fluctuating dramatically.

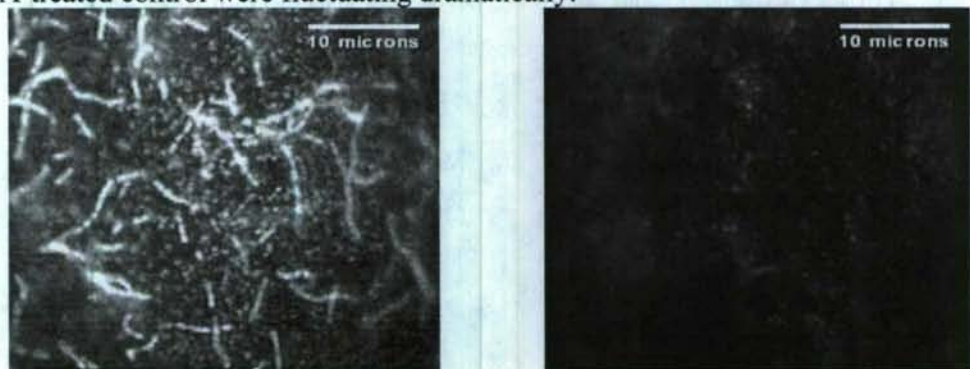


**Figure 4-1.** Surfaces treated with 1 $\mu$ M NEM-myosin and then 1% BSA (left) contained actin filaments on the surface after a wash of the sample, as seen in a TIRF microscope. A control surface, treated with only 1% BSA (right) contained no filaments attached to the surface. Filaments would come in and out of the TIRF range, but would not stick to the surface. Total actin concentration was 1  $\mu$ M and total Phalloidin concentration was 0.07  $\mu$ M.

**Characterization of Motility of ActA-coated Beads:** The velocity of 500-nm beads was characterized as follows. Motility assay mixtures were introduced into the NEM-myosin treated flow chambers. Once formed, actin-rich tails attached to the glass surface were distinguished from tails that were not attached in phase contrast by their decreased Brownian motion. Time lapse images were taken every 15 seconds for 5 minutes, and velocities were measured of those tails that were elongating on the surface. The average velocity for beads on the glass surface treated with a 0.1- $\mu$ M NEM-myosin solution was  $0.034 \pm 0.007$  microns/second. The average velocity for beads on the glass surface treated with a 1- $\mu$ M NEM-myosin solution was  $0.037 \pm 0.008$  microns/second. The difference in myosin concentration does not have an affect on the elongation of filaments in the rocket tail of 500-nm beads. Subsequently, it has no affect on the velocity of the 500-nm particle. Figure 4-2a shows a time lapse image of a motile bead on the glass cover slip surface treated with 0.1- $\mu$ M NEM-myosin solution. TIRF microscopy was used to confirm that actin rocket tails were attached to the surface. In TIRF, only 100 nm into the sample is visible. Therefore, the only way tails would be visible in TIRF would be if they were attached to the surface. Figure 4-2b shows the TIRF images of the slide, confirming that tails were on the surface.

To allow more samples to be taken simultaneously, the velocity of tail elongation of motile beads were further characterized while still in suspension using platelet extracts of varying dilution and found to be linear with total protein concentration, as shown in Figure 4-3.

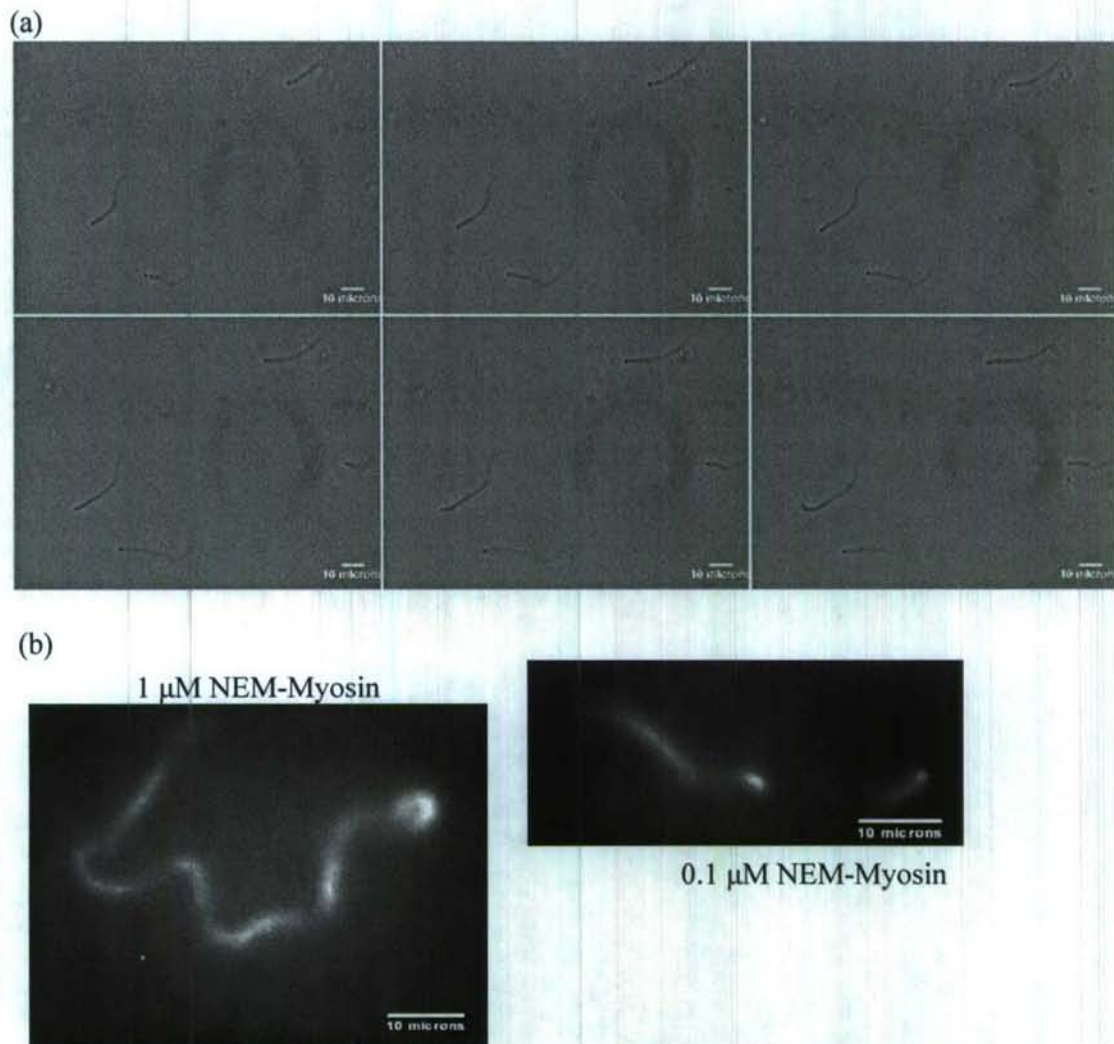


**Figure 4- 2.** (a) Sequence of time lapse images of 500 nm beads with tails in phase contrast. The glass surface was treated with 0.1  $\mu$ M NEM-myosin and the platelet extract motility assay. There are four 500 nm beads that are being pushed by their respective rocket tails. The average velocity for all the motile beads on 0.1  $\mu$ M NEM-myosin treated glass surfaces is  $0.034 \pm 0.007$  microns/second. Scale bar is 10 microns. (b) Glass surfaces treated with 1  $\mu$ M NEM-myosin (left) and 0.1  $\mu$ M NEM-myosin (right) as seen in TIRF microscopy show attachment of actin rocket tails on 500 nm beads to the surface. There was no difference in velocity of the 500 nm beads on the two surface treatments.

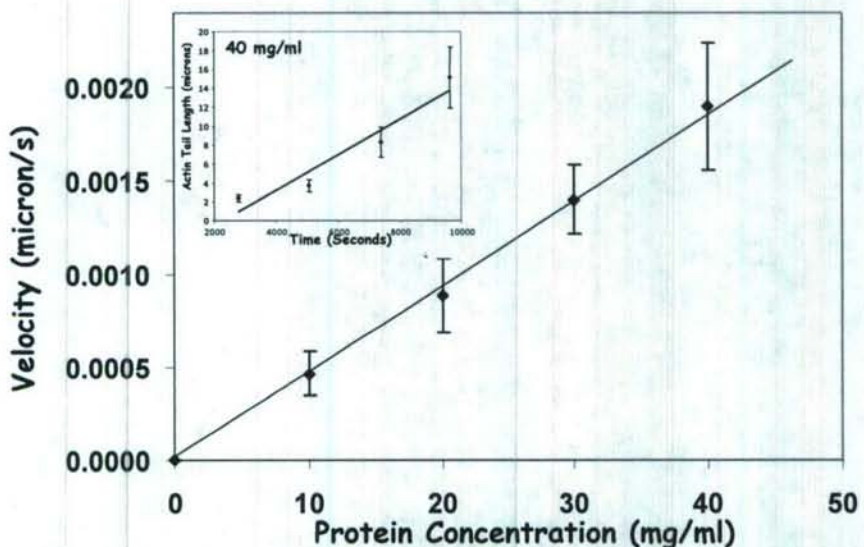


**Figure 4-3** - Speed of covalently-bound ActA-coated 500-nm particles as a function of total protein concentration in a platelet extract. Note the velocity was estimated from the mean tail length of an ensemble of particles over time (neglecting the rate of tail disassembly). (Note: Velocities were estimated from images of three-dimensional tails projected into the x-y plane; the actual tail length is expected to be a factor of about 2 larger than the projected tail length measured. As such, the reported velocities are expected to be two-fold lower than actual three-dimensional velocities.)

**Elongation of individual actin filaments on patterned surfaces** -- By using Polydimethylsiloxane (PDMS) stamps, we have quantified the ability of F-actin binding stripes of varying width to guide filament elongation. Although filaments in these studies were not bound to particles, we do not anticipate significant difference between free filaments and particle bound filaments ends because the particle size (~50 nm) will be much smaller than the characteristic filament lengths. Therefore, we take our success in guiding free-filaments is proof-of-principle that particle-bound filaments can be similarly guided.

PDMS stamps provided by Task 2 were used to stamp NEM-myosin onto glass surfaces. Hydrophilic stamps stored in water were dried under nitrogen and a 0.2- $\mu$ M NEM-myosin solution was immediately placed on the stamp. We incubated the stamps for 30 minutes in the NEM-myosin solution, and dried the stamp again under nitrogen. The stamps were placed down with the NEM-myosin side coming in contact with a cleaned glass cover slip and the glass cover slips were incubated with the stamp for 30 minutes. The stamps were then removed from the cover slips and the glass cover slips were converted into a flow chamber. The chamber was then washed first with a BSA solution in a high salt Tris-buffered saline solution (50 mM Tris-Cl, pH 7.6, 600 mM NaCl) at 1% w/v followed by a 1% BSA solution in low salt Tris-buffered saline (50 mM Tris-Cl, pH 7.6, 50 mM NaCl).

Actin filaments were formed using unlabeled and Alexa 488- labeled actin prepared from rabbit muscle, prepared in Task 1. Using the protocol in Kuhn and Pollard (Kuhn and Pollard 2005), 1.5- $\mu$ M actin (30% fluorescently labeled) was polymerized and actin filaments were placed in the flow chamber and immediately observed using TIRF microscopy. The pattern formed by NEM-myosin was visible in TIRF by an accumulation of fluorescently-labeled actin monomers on the patterned area.

Using the microcontact-printing procedure, we produced and characterized filament growth on myosin tracks of six different average widths ( $3.3 \pm 0.3$ ,  $4.3 \pm 0.5$ ,  $5.7 \pm 0.2$ ,  $10.7 \pm 1$ ,  $15.1 \pm 0.8$ ,  $20.2 \pm 0.5$   $\mu$ m). Fluorescence and AFM images were taken to assess the uniformity of NEM-myosin coverage. As shown in Figure 4-4A, the NEM-myosin regions were clearly delineated by the preferential non-specific adsorption of fluorescent actin monomers or oligomers with the NEM-myosin regions relative to the BSA regions. The magnified three-dimensional AFM image (Figure 4-4B) of a representative track edge shows a confluent protein layer, with thickness shown in Figure 4-4C. The measured thickness variation of the protein layer is comparable to the 7-nm diameter of a single actin filament, implying that the peaks and valleys of the layer should have little effect on the guidance of the filaments.

The microcontact-printed surfaces were exposed to the actin solution, allowing subsequent capture of nascent filaments from solution by the NEM-myosin-coated regions with the majority of captured filaments continuing to elongate on the surface. (Surfaces stamped with 0.5 mg/mL BSA showed little evidence of filament binding.) We were able to monitor (+)-end filament elongation on the NEM-myosin tracks in real-time using TIRF microscopy (Figure 4-5). Notably, the tips of myosin-bound filaments clearly undulate during elongation, and the filaments continue to bind to NEM-myosin along their length as they extend. While filament segments were found both on the tracks and on the BSA-coated regions, filament segments on the BSA regions underwent larger thermal undulations (observed in the x- and y-direction) than those confined on the NEM-myosin track, indicating that filaments were tightly bound only to the NEM-myosin tracks. Filaments initially bound to the track either remained in the NEM-myosin region or elongated beyond the track edge, with the filament end continuing to elongate and undulate over the BSA-coated region. In many cases, these undulations allowed a filament which had crossed the boundary of the NEM-myosin track at a glancing angle to rebind to the track, now with the filament end often aligned with the track direction (Figure 4-6).

The resulting alignment of the filaments with the track edge was quantified by measuring the angle  $\theta$  for segments along each of several filaments for each track width (Figure 4-7A) and calculating the mean of  $\cos(2\theta)$ . Filament alignment on the narrower track widths was found to be significant and the degree of alignment increased as the track width decreased (Figure 4-7B, solid squares). To determine whether alignment resulted primarily from interactions with track boundaries, the mean of  $\cos(2\theta)$  was recalculated for the subset of filaments within approximately 1.5  $\mu$ m of the track edge on the tracks wider than 3  $\mu$ m (Figure 4-7B, open squares). The filaments near the track boundaries had a similar average alignment for each track width, but the relative number of these edge filaments was too few to generate a significant overall average alignment for the larger track widths. These observed trends are consistent with the interpretation that filaments in tracks with widths comparable to the filament persistence length ( $\sim 10$

$\mu\text{m}$ ) take random walk trajectories within the boundaries of the track and only become aligned when encountering the track boundary. On the other hand, filaments in tracks that are small relative to the filament persistence length encounter the track boundary and become realigned before significant changes in direction occur (Figure 4-7C).

The probability of realignment of a filament with the track edge is also dependent on the alignment of the filament immediately before crossing the NEM-myosin track edge. The histogram in Figure 4-8 demonstrates that at smaller alignment angles, these rebinding events were more frequent, ranging from  $\sim 90\%$  recapture-probability for angles less than  $15^\circ$  decreasing to zero probability at angles greater than  $60^\circ$ . From this result, we surmise that the bending energy at large angles required to recapture a filament is too large to be achieved by thermal undulations.

We also investigated the effect of NEM-myosin concentration used to treat the PDMS stamps (Task 3) on the alignment of elongating filaments. As shown in Figure 4-9A, the degree of alignment, again quantified by the mean  $\cos(2\theta)$ , trended upward with NEM-myosin treatment concentration, with the degree of alignment on tracks prepared with the highest concentration tested ( $2 \mu\text{M}$ ) significantly greater than that of the lowest ( $0.1 \mu\text{M}$ ), the latter of which failed to generate statistically significant alignment. These results suggest that lower NEM-myosin surface densities are less efficient at recapturing undulating filament ends that have elongated off the track edge. Finally, we anticipated that at higher densities, myosin might bind at or near the filament (+)-ends, and thereby hinder monomer incorporation. To determine the effect of myosin concentration, we measured the elongation rate of filaments on the protein tracks prepared with varying NEM-myosin concentrations used in Figure 4-9A. As shown in Figure 4-9B, the elongation rate decreased only slightly for the highest myosin concentration, implying that the NEM-myosin had little effect on actin polymerization.

These data demonstrate that microcontact printing can be used as an effective way for guiding the polymerization of actin filaments. By printing NEM-myosin tracks on glass surfaces, actin filament binding was confined to certain regions of a substratum and aligned by controlling the path of filament elongation. Smaller track widths provided the greatest degree of alignment by increasing the frequency of elongating ends encountering the track boundaries, whereupon the filament elongation direction tended to preferentially align with the edge of the NEM-myosin tracks, and alignment appeared to be confined primarily to the track boundaries. The degree of alignment, but not the polymerization rate, depended on the concentration of NEM-myosin used to prepare the stamp, with the lowest concentration ( $0.1 \mu\text{M}$ ) generating little, if any, alignment. Notably, this lower value is near the minimum concentration needed to provide a monolayer on the PDMS stamp, hence it is likely that, in this case, less than a confluent layer was transferred upon printing.

Taken together, our results can be explained by the following alignment mechanism (Figure 7). Nascent filaments are captured on the track surface and elongate on the NEM-myosin. As a filament elongates, the newly polymerized portion is quickly captured by the myosin surface until the filament end reaches the NEM-myosin track boundary. The filament continues to grow across the boundary while unattached to the substratum and becomes capable of undergoing larger thermal undulations. These undulations allow the filament to be recaptured to the track in a more aligned direction, provided the angle at which the filament encounters the track boundary is sufficiently

small, and the myosin surface density is sufficiently large, to allow NEM-myosin in the track to rebind the undulating filament end. Our findings suggest that at narrower track widths than measured here, even greater alignment would be achieved, with greatest alignment occurring when the myosin track widths approach the filament width.

Our results indicate that filament-binding tracks are a viable method for guiding the direction of filament elongation on surfaces *in vitro*, including guidance of molecular shuttles bound to the elongating filament (+)-ends. Because elongation is guided by filament undulations and filament binding to the track, we would expect similar guidance of elongating filaments with or without particles bound to the filament ends, provided the particles are small enough not to interfere with the undulating end.

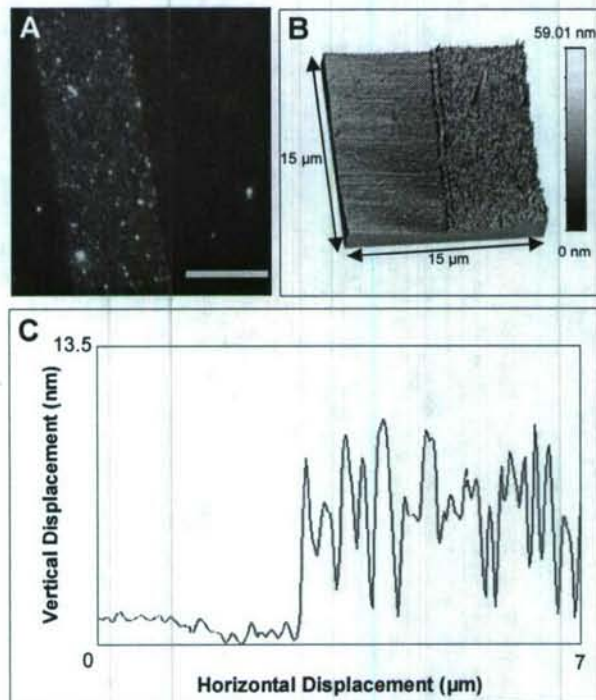


**Figure 4-4.** Images of microcontact-printed myosin tracks on a glass coverslip. (A) TIRF image of NEM-myosin track (brighter region slightly right of center) delineated by nonspecific adsorption of fluorescently-labeled actin monomers to adsorbed NEM-myosin (scale bar = 10  $\mu$ m). (B) Topographic AFM image of track edge showing uniformity of NEM-myosin coverage. (C) Line-scan of vertical displacement versus horizontal displacement from plot B. The height of the step-edge was found to be approximately 8 nm and the peak-to-valley height variations in the NEM-myosin region were found to be on the order of 4.4 nm. From (Interliggi et al. 2007).

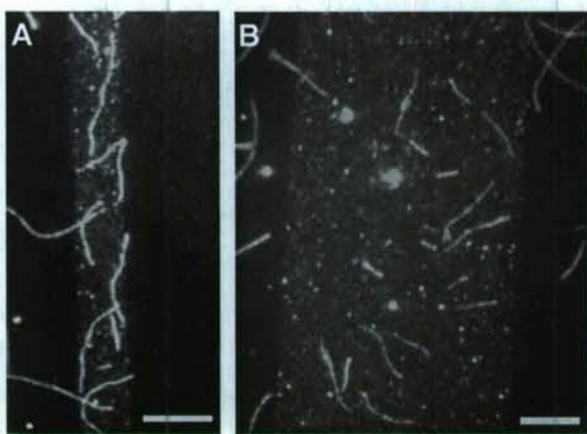


**Figure 4-5.** TIRFM images of elongating actin filaments on NEM-myosin tracks of approximately 3.7  $\mu\text{m}$  (A) and 19.5  $\mu\text{m}$  (B) widths. Images were taken approximately 48 min and 22 min after initiation of polymerization, respectively (1.5  $\mu\text{M}$  actin, 15% Alexa 488-labeled actin). Scale bars = 5  $\mu\text{m}$ . From (Interliggi et al. 2007).

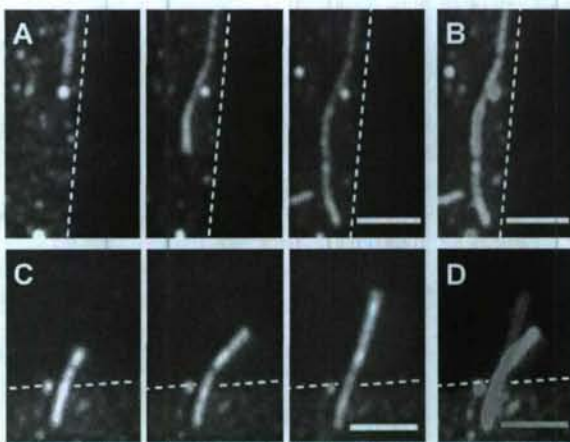


**Figure 4-6.** TIRFM images showing undulating ends of elongating filaments. (A) Images from a time-lapse sequence for a filament end elongating within a NEM-myosin track (time interval = 195 sec; dashed-line indicates track edge). (B) Composite of images from (A), indicating small undulations away from the ultimate filament trajectory when elongating on NEM-myosin. (C) Images from a time-lapse sequence for a filament elongating across the track edge and into the BSA region (time interval = 100 sec). (D) Composite of images from (C), indicating larger undulations of the filament end over the non-binding BSA surface. Scale bars = 2  $\mu\text{m}$ . From (Interliggi et al. 2007).

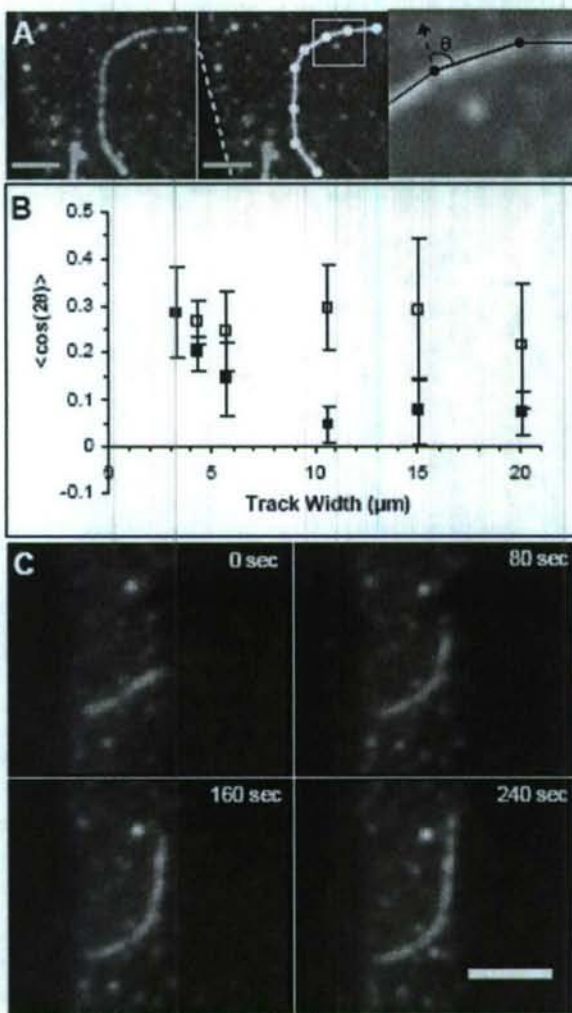


**Figure 4-7.** Effect of track width on filament alignment. (A) Example of filament segmentation to estimate orientation angle  $\theta$  with track edge. Left: Original TIRFM image; Middle: Same image showing filament segments; Right: Enlargement of boxed region in middle image showing how  $\theta$  was determined for each individual segment. Scale bar = 2  $\mu\text{m}$ . (B) Solid squares represent the degree of filament alignment with NEM-myosin tracks versus track width. The error bars represent the weighted standard error among independent samples for each track width. Significant filament alignment was present in the three narrowest track widths (3.3  $\mu\text{m}$ :  $n = 16$ ,  $p = 0.005$ ; 4.3  $\mu\text{m}$ :  $n = 36$ ,  $p < 0.0001$ ; 5.7  $\mu\text{m}$ :  $n = 14$ ,  $p = 0.042$ ; 10.7  $\mu\text{m}$ :  $n = 17$ ,  $p = 0.11$ ; 15.1  $\mu\text{m}$ :  $n = 19$ ,  $p = 0.14$ ; 20.2  $\mu\text{m}$ :  $n = 10$ ,  $p = 0.051$ ). Open squares represent the alignment of filaments within approximately 1.5  $\mu\text{m}$  of the track edge (4.3  $\mu\text{m}$ :  $n = 36$ ,  $p < 0.0001$ ; 5.7  $\mu\text{m}$ :  $n = 14$ ,  $p = 0.006$ ; 10.7  $\mu\text{m}$ :  $n = 15$ ,  $p = 0.003$ ; 15.1  $\mu\text{m}$ :  $n = 12$ ,  $p = 0.049$ ; 20.2  $\mu\text{m}$ :  $n = 7$ ,  $p = 0.080$ ). (C) Time-lapse sequence showing the alignment process for an elongating filament (+)-end at the track edge. Scale bar = 2  $\mu\text{m}$ . From (Interliggi et al. 2007).

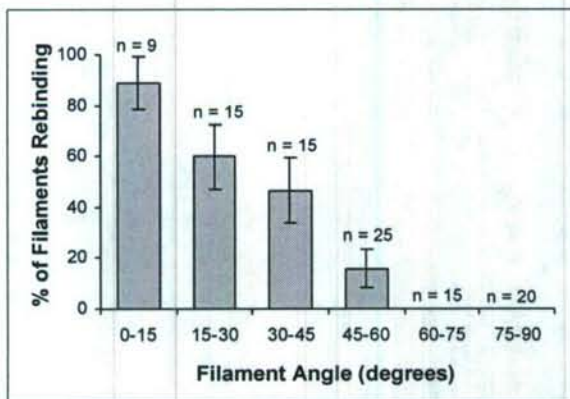


**Figure 4-8.** Histogram showing that the probability of rebinding and filament alignment with track depends on angle of incidence with track edge. Error bars represent  $\pm$  standard error =  $(p(1-p)/N)^{0.5}$ . Note: No filaments crossing the track at  $\theta > 60^\circ$  were observed to rebind to the NEM-myosin track. From (Interliggi et al. 2007).

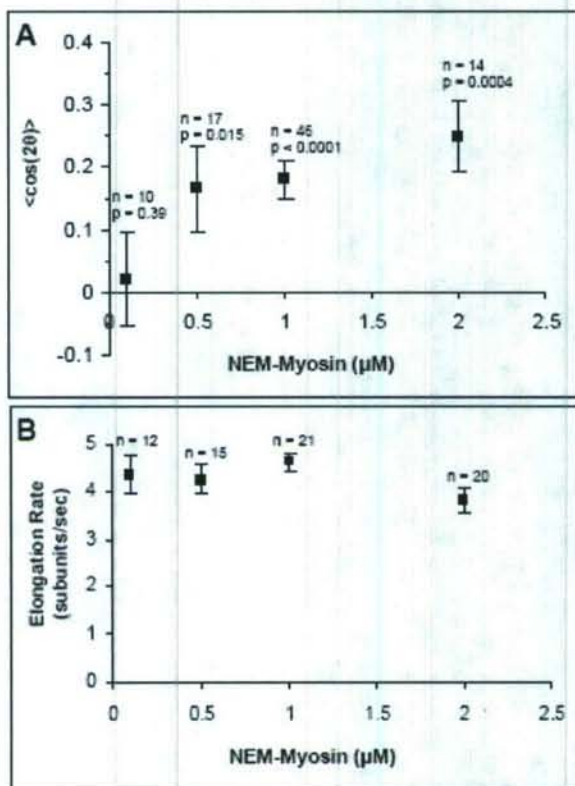


**Figure 4-9.** Dependence of filament alignment and elongation rate on the concentration of NEM-myosin used for microcontact printing (average track width =  $4.6 \pm 0.6 \mu\text{m}$ ). (A) Alignment appears to decrease for 0.1  $\mu\text{M}$  NEM-myosin treatment condition. The error bars represent the standard error among independent samples for each myosin concentration. All treatments except 0.1  $\mu\text{M}$  NEM-myosin provided significant alignment of filaments ( $n$  = number of tracks,  $p$  = one-tailed  $p$ -value). Additionally, the 2  $\mu\text{M}$  and 0.1  $\mu\text{M}$  samples were statistically different from each other ( $p = 0.021$ ). (B) Filament elongation rate is insensitive to changes in NEM-myosin concentration used in printing (0.75  $\mu\text{M}$  actin, 15% rhodamine-labeled actin;  $n$  = number of filaments that instantaneous velocities were measured,  $p$ -value = 0.17 when comparing all means). The error bars represent the standard error among instantaneous elongation rates for each myosin concentration. From (Interliggi et al. 2007).

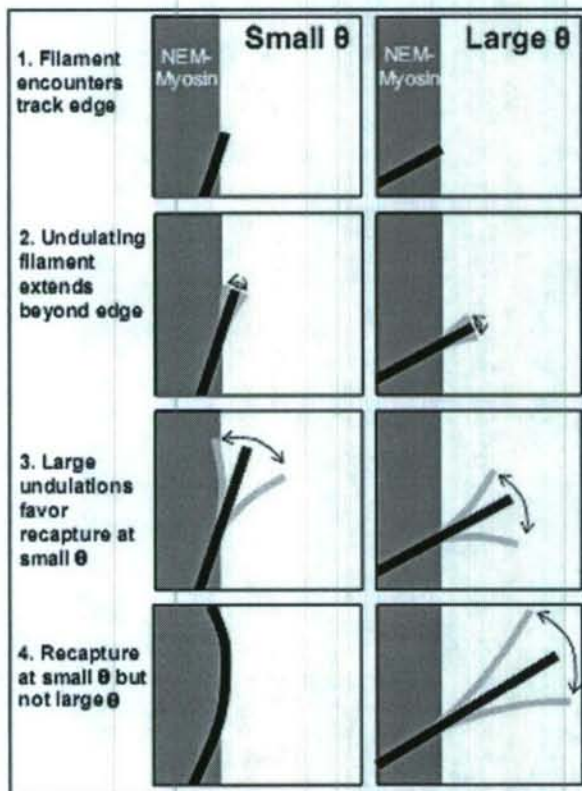


**Figure 4-10.** Illustration of the likely mechanism for actin filament alignment on NEM-myosin tracks. Elongating filament ends first encounter (1) and then undulate over (2) the track edge. The increase in filament length over the track causes larger undulations to occur (3). Finally (4), the filament either is recaptured by the track for smaller  $\theta$ , or continues to elongate away from the track for larger  $\theta$ . From (Interliggi et al. 2007).

**Characterization of Single-Filament Actuators** – We quantified the ability of 50-nm beads (Task 1) to produce single filaments by insertional polymerization. To determine the incubation time necessary to achieve one filament per bead, a time study was done by incubating the beads with a motility assay for 1 minute, 2 minutes, 5 minutes, 10 minutes, 20 minutes, and 35 minutes. Due to the large number of filaments observed on the beads at time points 20 minutes and 35 minutes, only time points 1 minute thru 10 minutes were analyzed.

To prevent human bias, 25 random images at each time point were taken. For each image, number of particles, filament length, and number of filaments per particle were measured. The average filament length was not statistically different between the four time points. The histogram of filament lengths is shown in Figure 4-11. For filament lengths larger than ~100 nm, the distribution appears to be exponential which is consistent with a Poisson distribution of elongation times. The lower counts of shorter filaments less than 100 nm suggest that filaments grow for several subunits before stopping. At each time point the average filament length is ~500 nm, but based on particle velocities, a length of 500 nm would correspond to 10 seconds of growth. Velocities correspond to the growth rate of an ensemble of filaments where some filaments could be lagging, slowing the overall growth rate so single filaments could possibly be elongating at even faster rates. Therefore we can surmise that the majority of filaments have stopped growing by the time of fixation consistent with the reported histogram (Figure 4-11).

The average filament number per particle increased over time, due to new filaments initiating and polymerizing from the surface (Figure 4-12). To quantify the apparent increase of filaments, the number of filaments was normalized to the number of beads which resulted in a steady increase of filaments per bead (Figure 4-13). Next we quantified free filaments and found on average 7% of observed filaments were not bound to any bead (Figure 4-13). The histogram in Figure 4-14 shows the number of filaments per bead increases due to longer incubation times. To confirm ActA coated beads are initiating filament growth, the same motility experiment was tested replacing ActA coated beads with APES/glutaraldehyde treated beads. No filaments were observed on beads or on the substrate surface. Analysis of several hundred images and several thousand single filaments attached to beads (see Aim 1) shows a persistent attachment of filaments to particles. These filaments reached a steady-state polymerization rate within a few minutes. The observed filament lengths ranged from 100 nm up to 4  $\mu$ m. In order for a filament to polymerize to a length of 4  $\mu$ m at a growth rate of about 3  $\mu$ m/min, the filament must be associated with the bead for 1,400 monomer additions over more than a minute time period. The distribution in filament lengths, with the exception of fewer numbers of shorter filaments, can be explained by filaments nucleating and ceasing elongation at random times with constant rates. The fewer shorter filaments suggests filaments grow for many cycles before stopping. Shorter filaments either nucleated at a later time in the incubation period, or possibly the motor protein (ActA-VASP) was phosphorylated preventing continued filament elongation, or some other unknown cause stopped polymerization. Even though filaments have stopped elongating after a relatively short period, (on average ~10 s before elongation has stopped) the filaments are still strongly associated with the bead surface even after the several washes and treatments for EM. Single filaments emanating from 50 nm beads before EM treatment and fixation are

observed using total internal fluorescence microscopy (TIRF) (Figure 4-14) suggesting filaments are not being detached from the beads due to further treatments.

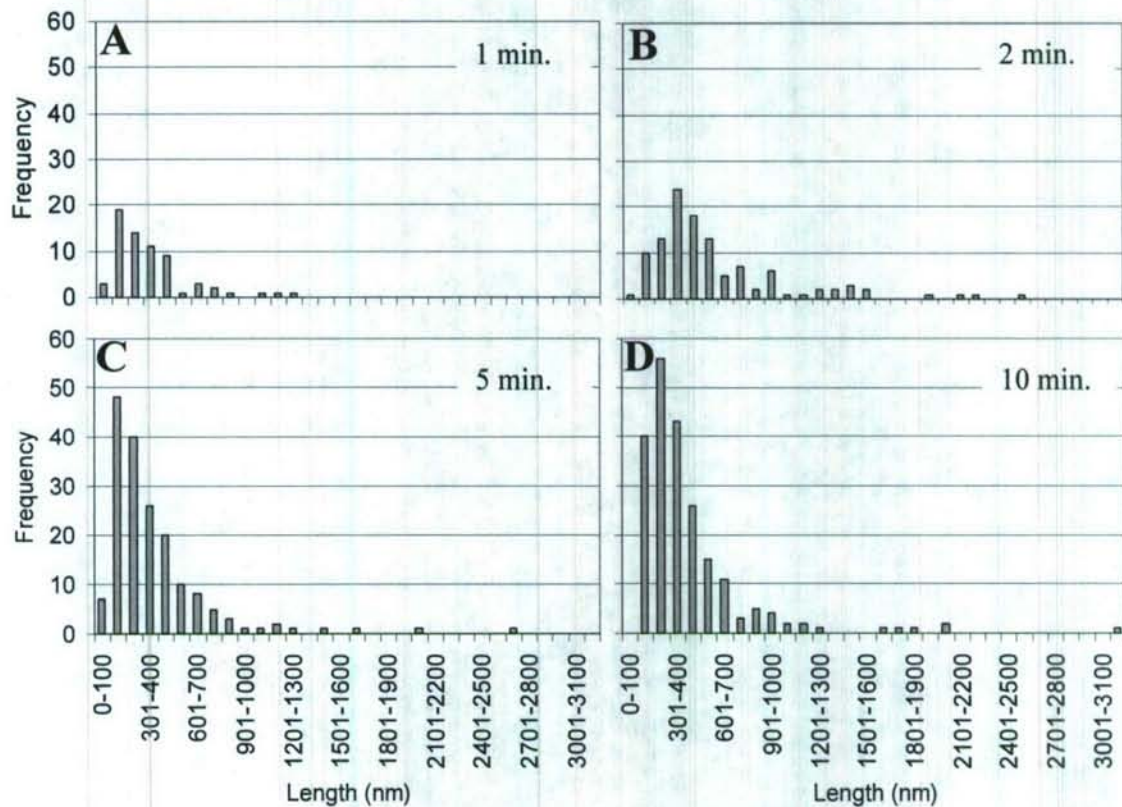


Figure 4-11 Histogram of filament lengths with bin size of 100 nm. A) One minute actin polymerization with 66 filaments. B) Two minute actin polymerization with 117 filaments. C) Five minute actin polymerization with 180 filaments (one outlier of 4.7  $\mu$ m not shown on graph). D) Ten minute actin polymerization with 215 filaments. Graphs A, B, and D have the same axes values as graph C. From (Sturm 2007).

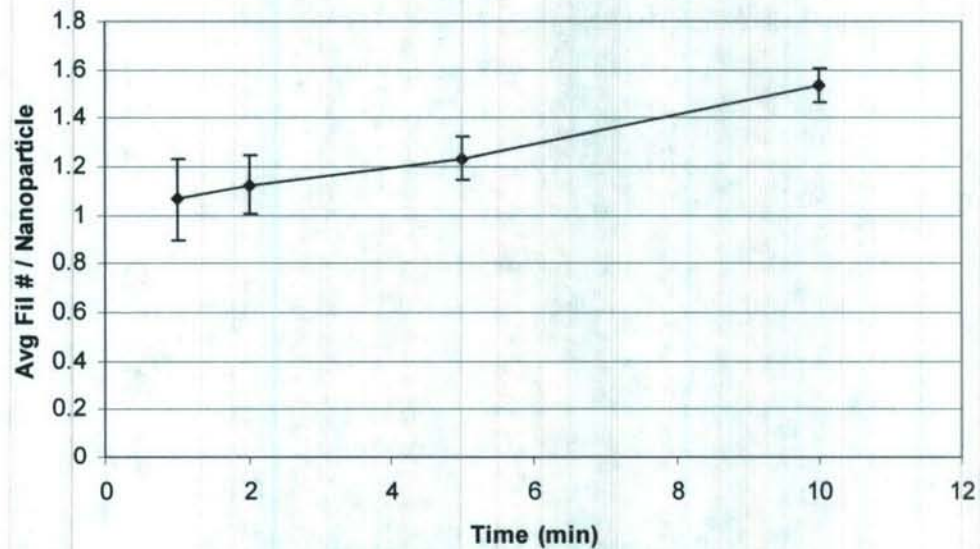


Figure 4-12. Average filament number per bead versus time. From (Sturm 2007).

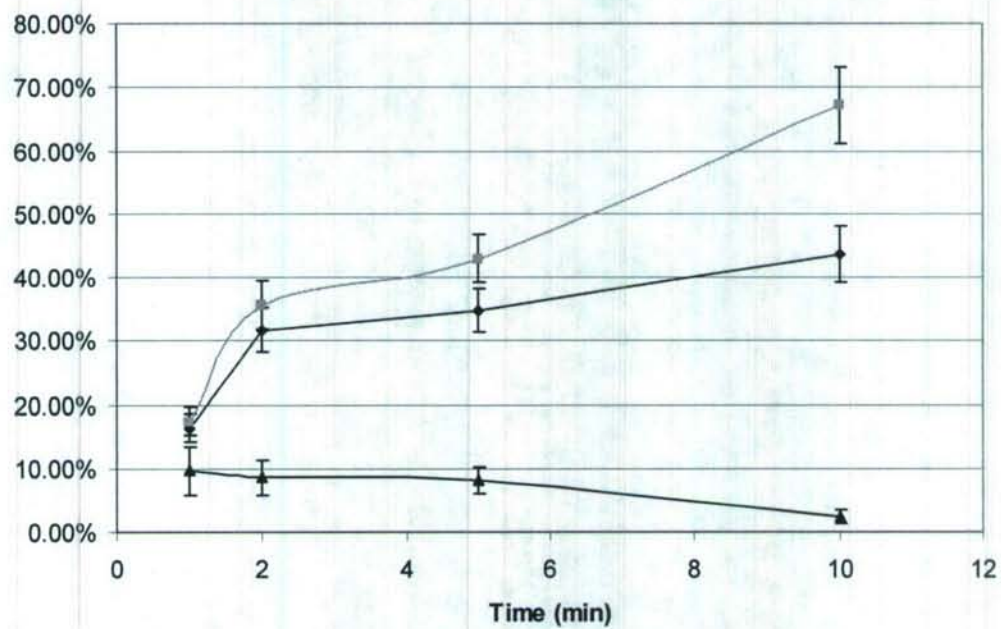


Figure 4-13 Number of filaments normalized to the total number of beads versus time. Blue diamonds are beads with filaments per total bead count, pink squares are number of bead associated filaments per total bead count, and black triangles are free filaments per total number of filaments. From (Sturm 2007).

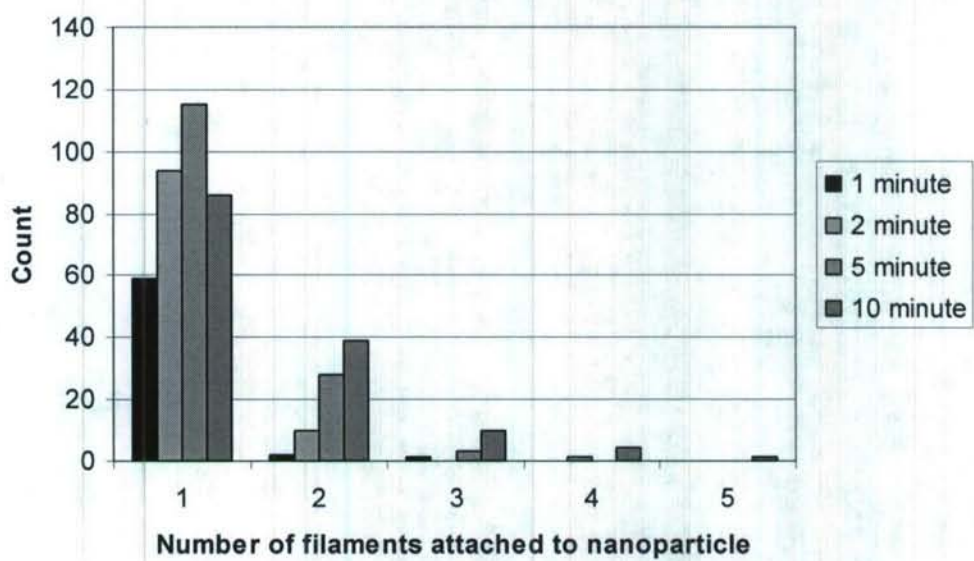


Figure 4-14 Histogram of the number of filaments attached to a bead versus time. From (Sturm 2007).

### Two-color fluorescence analysis of single-filament insertional polymerization

Although EM provides nanometer details, the system is not dynamic and polarity of the filaments can not be easily determined. Determining filament polarity was important to establish whether filament plus-ends are attached and elongating by insertional polymerization at the bead surface, as would be expected in an end tracking motor such as ActA·VASP, or instead minus-ends are attached and filaments are growing with free ends away from the beads. Our strategy for determining at which end actin is adding onto tethered filaments was to expose the bound ActA-functionalized beads to a cell extract containing fluorescent actin of one color for a few minutes, then switch to an extract containing actin of another color for a few minutes. The resulting filaments were then observed under total internal reflection fluorescence (TIRF) microscopy

Figure 4-15 illustrates some possible outcomes of a two-color single actin filament experiment, here assuming green actin is added first followed by red actin. If the elongating (+)-end is located at the bead surface, a span of red F-actin would appear next to the bead adjacent to green span farther from the bead (Figure 4-15A). On the other hand, if the (-)-end is bound to the bead surface; the colors would be reversed with the green span bound to the bead (Figure 4-15B). A similar result would appear if the filament were initially side-bound to the bead (Figure 4-15C), in which case green filament spans would appear on both sides of the bead and red adjacent to one span. It is also possible that the filament both nucleates and stops elongating while exposed to one color or the other, thereby producing a filament of uniform color (Figure 4-15D). Finally, two separate filaments could polymerize from the surface of the bead but overlap and appear indistinguishable as one filament. If the two filaments were of different colors, the conjoined filaments would appear as a yellow filament adjacent to the bead and the single-filament span would either red or green away from the bead, depending on whether the longer filament grew before or after the color change (Figure 4-15E). These possible outcomes are assuming negligible (-)-end growth or shrinkage from ATP-actin or ADP-actin.

### Color Change Assay

ActA functionalized 50 nm beads were bound to a flow chamber as described above. Actin was labeled with either Oregon-green or rhodamine. A motility assay with 5  $\mu$ M non-labeled actin (black actin) was flowed through the chamber for 2 minutes. Then, a motility assay with 5  $\mu$ M Oregon-green actin (green actin) was flowed through the chamber for 1 to 2 minutes. Next, a motility assay with 5  $\mu$ M rhodamine actin (red actin) was flowed through the chamber for 1 to 2 minutes. The order of actin addition to the flow chamber did not prevent intercalation of actin monomers to produce two color single filaments. Last, 1% glutaraldehyde was flowed through the chamber to fix the filaments. Samples were viewed within 1 minute of preparation using TIRF.

**Results from Two-color Filament Analysis** - There were several criteria for counting individual filaments. Filaments had to be sufficient length ( $>1 \mu$ m), filaments could not overlap with other filaments at critical points such as color change points or bead-filament attachment, filaments had to have a high signal to noise ratio and the filament had to be continuous, the position of labeled filamentous actin did not overlap with other labeled filamentous actin except minimally at the transition of the color change. These

same criteria were used for counting single color filaments (when applicable). Some of the filaments appear to have variations in the fluorescence intensity. This could be from background autofluorescence of protein from the extract or from the amount of fluorescence monomer incorporated at any point in the filament. Filaments could also fluctuate from the surface reducing the fluorescent signal output generated from the evanescent wave of TIRF. Figure 4-16 is a compilation of all 158 two color single filaments observed in more than 150 image sets of 12 experiments. Approximately 20 of the 158 events were considered to be of excellent quality meeting all criteria. Figure 4-17 shows a two color filament bound to a bead where Oregon-green was added first and rhodamine actin followed. Both fluorescent channels are shown separately and a graph of the line scan along the filament shows the normalized fluorescence intensity. The graph of the line scan clearly shows a fluorescence intensity switch from the bead to the end of the tail. The green portion of the filament is clearly not connected to the bead by green actin. Figure 4-18 is a histogram of bead and filament count for 20 image sets. Twenty-five percent of beads had single actin filaments and 11% to 12% of beads counted had single filaments with 8% of the single filaments having two fluorescent actin monomers incorporated. To test that filaments were being generated by ActA beads, the same two-color experiments were performed as before except ActA coated beads were replaced with BSA coated beads. Beads were also completely removed and a motility assay containing actin was added to the flow chamber as before. No filaments were observed in either of the controls.

Over 158 events show a bead with a two color single actin filament attached. Every event that exhibited a two color actin filament resulted in the correct polarity of (+)-end closest to the bead independent of order of fluorescent actin added. Approximately 25% of beads counted had an actin filament attached compared to 35% observed in EM images at a comparable time of polymerization (5 minutes). The difference in observed filaments is due to the resolution limit of TIRF compared to EM. A criteria of filaments being around 1  $\mu\text{m}$  or greater was set for counting filaments in TIRF. The length criterion of a single filament in EM was much lower because filaments are easier to distinguish due to the high resolution associated with EM.

Single filaments with only one color actin were ~11% out of beads counted for either color and independent of the order of fluorescent addition to samples. Out of the single filaments counted 8% were two color filaments. At first glance these numbers may seem low but can be explained from the results of EM. From the known elongation rate (~3  $\mu\text{m}/\text{min}$ ), the average filament (~500 nm) measured in EM would only elongate for 10 seconds. Few filaments in EM were observed to elongate for much longer times and distances (max ~4  $\mu\text{m}$ ) for unknown reasons (phosphorylation of VASP may not have occurred until a later time or some other poisoning device had not happened). Assuming the same mechanism is occurring in these TIRF experiments, filaments grow for 10 to 20 seconds and stop elongating but still remain persistently attached (two chamber flow through before fixation). The addition of another fluorescent actin would then not intercalate into the halted filament. Halted filaments would also explain the low occurrence of two color single filaments. For a two color filament to occur, the filament must have started elongating in the few seconds remaining before the next fluorescent actin is added and the filament must continue to intercalate the new actin.

The observation of new actin monomers intercalating at the surface of a bead shows single actin filaments are persistently attached while actin is insertionally polymerized. Free filament models do not have an explanation to support this observation. A free filament would easily diffuse away from a bead surface during the 10 to 20 seconds of actin polymerization observed in EM and TIRF. Insertional polymerization from ActA-coated beads strongly suggests elongation by end-tracking motors and supports the actoclampin model for ActA·VASP. Further experiments are required to establish that VASP (rather than, e.g., adsorbed formin) is the end-tracking protein responsible for actin assembly in these experiments.

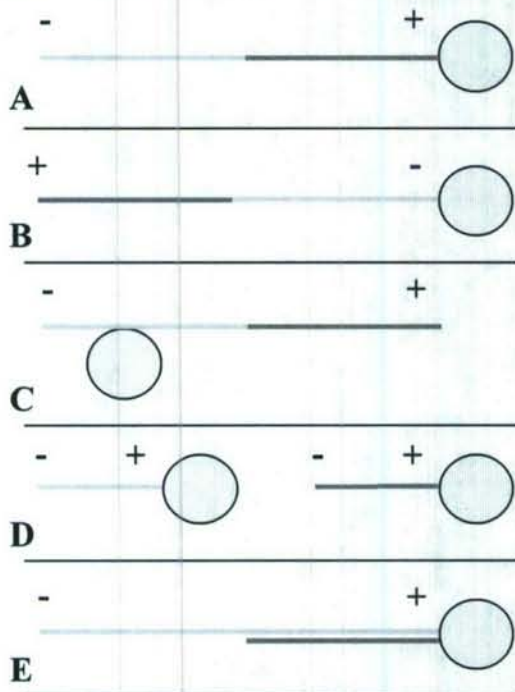


Figure 4-15 - Fluorescent actin change hypothetical scenarios with green added to the assay first, then red, attached to a yellow 50 nm bead. The + and - designate the (+)-end and (-)-end of the filament. A) Result if insertional actin polymerization is occurring. B) Result if the actin filament is nucleated in solution and bound to the bead with the incorrect polarity. C) Filament nucleated in solution and bound to the side of the bead. D) Single filament growth without incorporation of two colors. E) Overlap of filaments giving the appearance of A, except the red/green overlap would create a yellow filament. From (Sturm 2007).

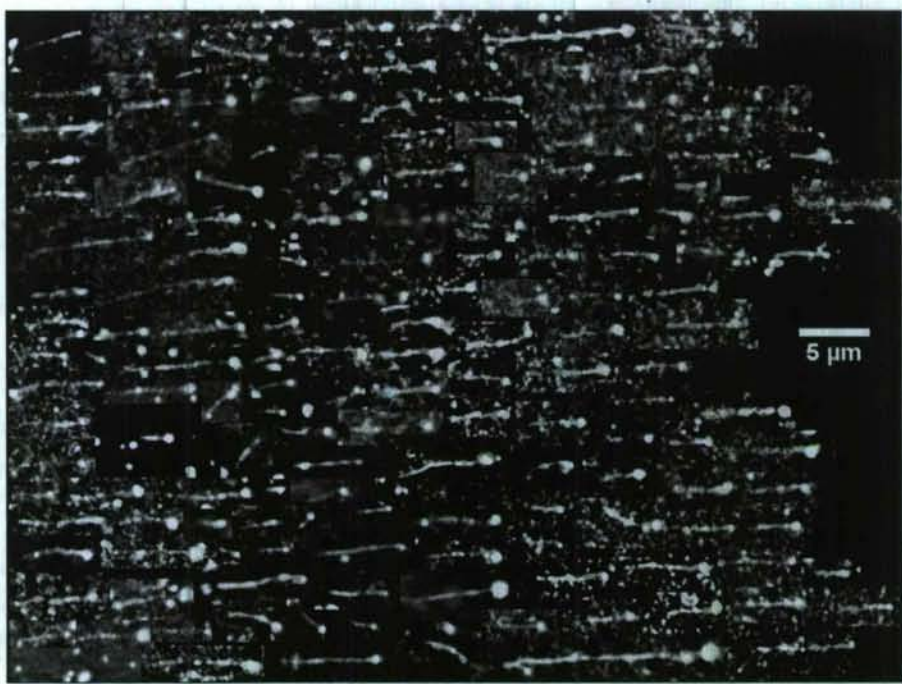


Figure 4-16. Compilation of 158 color change events observed from 12 experiments and more than 150 image sets. From (Sturm 2007).

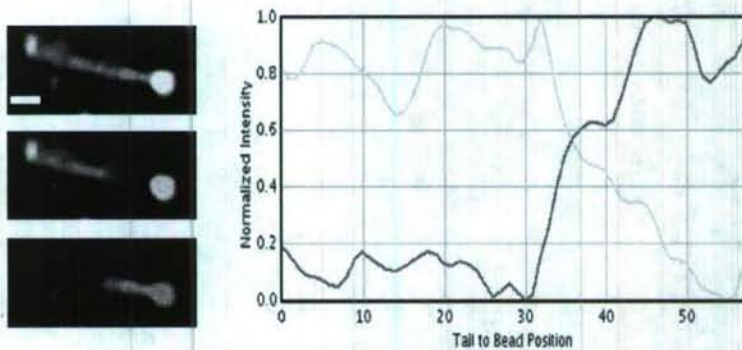


Figure 4-17. Both fluorescent channels and overlay of a two color filament where Oregon-green actin was added to the experiment first. The graph is of a line scan along the length of the filament. Scale bar = 1  $\mu$ m. From (Sturm 2007).

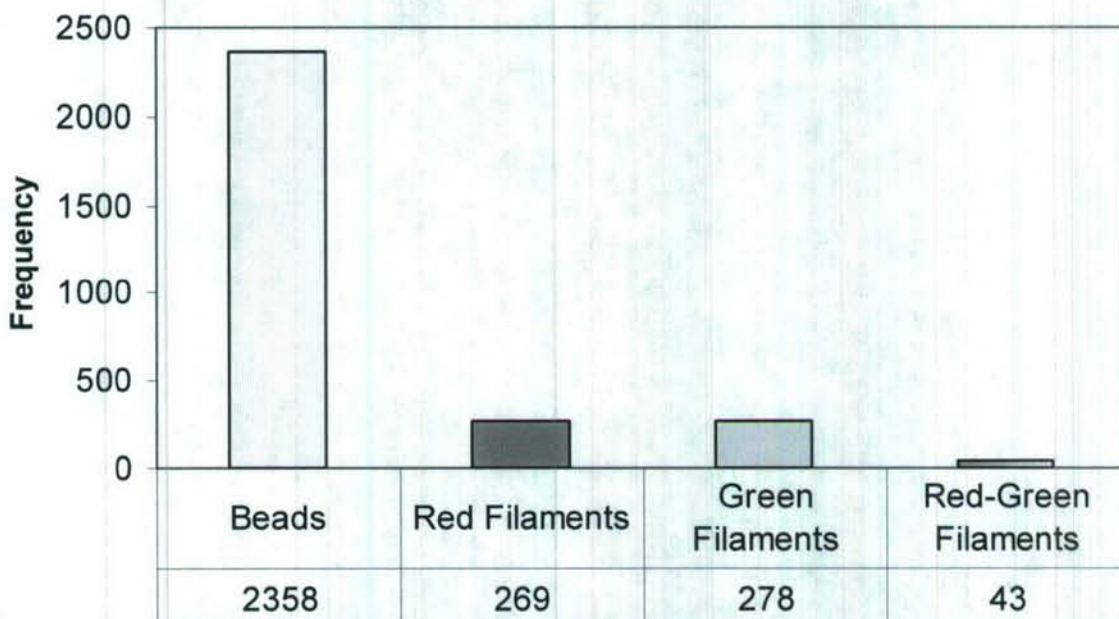


Figure 4-18. Histogram for beads and filaments of 20 image sets. From (Sturm 2007)

**Modeling Propulsion by End-Tracking Motors** – We developed a mathematical model for particle propulsion by filament-end tracking motors. In particular, we explored the rate-limitations of propulsion, which can be modeled as a reaction-diffusion problem: actin monomers must diffuse to the particle surface, before being incorporated into the filament end (considered the reaction step) by the filament-end tracking mechanism. It was anticipated that at sufficient density of filament ends at the surface, diffusion would become rate-limiting due to rapid consumption of monomer as well as hindered diffusion through the actin network. A concentration profile decreasing toward the center of the actin tail is predicted (Figure 4-19), with the concentration at the tail center decreasing with increasing particle radius. This model allows estimation of the particle velocity as a function of particle radius and monomer concentration, and predicts a linear relationship with monomer concentration for conditions used here, consistent with data in Figure 4-20. Predictions of particle-size dependence agree closely with literature measurements, as shown in Figure 4-7. We published this analysis in the Biophysical Journal (Dickinson and Purich 2006).

Although the molecular details of ActA-VASP end-tracking motor complexes are not yet well-characterized, we developed a generalized model to predict the elongation rate versus load for end-tracking proteins of different tracking protein stiffness. We also explored different kinetic limits of the end-tracking polymerization cycles. This analysis was published in the Appendix of a recent Biophysical journal paper (Dickinson and Purich 2006).

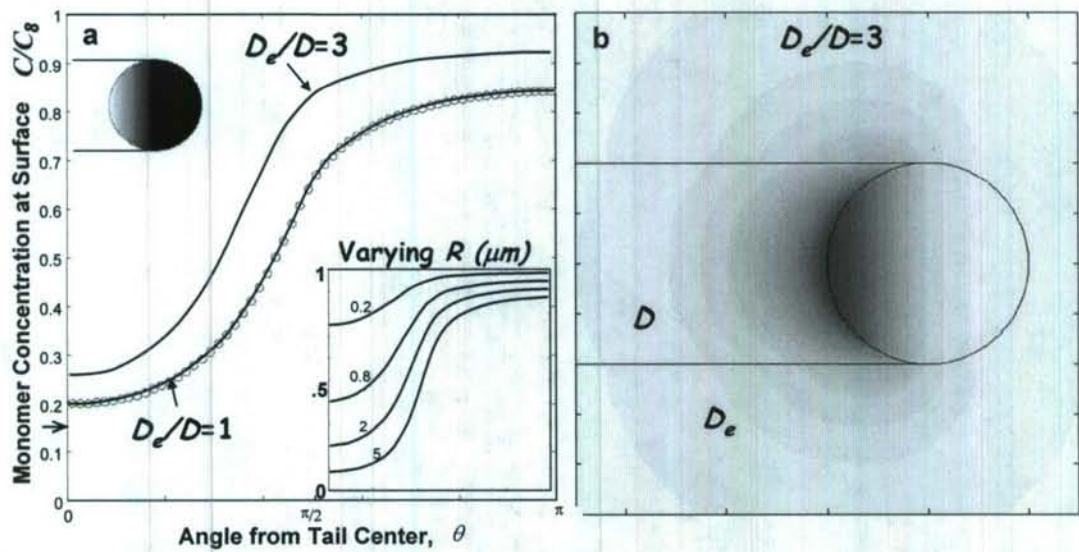


Figure 4-19 -- Model predictions of monomer concentration gradients based on reaction-diffusion model, shown as concentration-versus angle from center of the tail; and (b) contour plot where grey level corresponds to actin concentration.  $D$  and  $D_e$  actin monomer diffusion coefficients inside and outside respectively.  $R$  is the particle radius. (from (Dickinson and Purich 2006)).

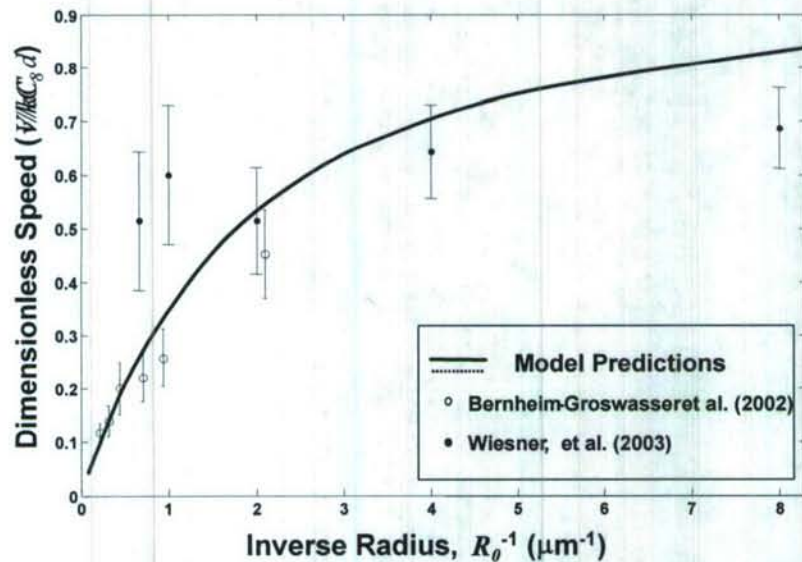


Figure 4-20 -- Model predictions of particle speed compared to experimental data (Bernheim-Groswasser et al. 2002; Wiesner, et al. 2003). Plot from (Dickinson and Purich 2006).

## **Task 5 - Direct real-time detection of protein-protein interactions in signal transduction pathways**

Denis Wirtz and Melissa Thompson, Johns Hopkins University

### **A. Introduction**

In vivo and in vitro visualization of biological events using organic and genetically encoded protein is a very powerful technical approach that has been developed and refined in the last three decades. However, progress in this area has been limited and sometimes difficult due inherent properties of these fluorophores, such as broad absorption and emission spectra and rather low photobleaching thresholds. Luminescent semiconductor nanocrystals (quantum dots, QDs), such as those made of CdSe-ZnS core-shell nanoparticles, are inorganic fluorophores with unique properties that allow them to circumvent many of the photophysical limitations encountered by conventional fluorophores. QDs have high quantum yield (QY), tunable narrow and symmetric emission and broad excitation spectra, which allow use of a single wavelength to simultaneously excite and image QDs with differing emissions. QDs also have exceptional resistance to photo- and chemical degradation and very high photobleaching thresholds. However, despite the intense interest that the development of QD bioconjugates has generated in the past five years and the availability of two commercial sources for luminescent QDs, there is still a tremendous amount of work to be done in order to harvest the large potential utility of using these inorganic fluorophores in bio-oriented applications and investigations. There is a clear need to develop hydrophilic QD probes that are homogeneous, highly luminescent, stable and functional. For example, the harsh and complex cytoplasmic and cellular compartments in live cells require one to use nanocrystals that are stable not only in high ionic strength conditions but also over a broad range of pH. QDs should also be biocompatible and have minimal or no toxic effects to cell functions and developments. Moreover, such hydrophilic QDs should offer one the ability to functionalize their surfaces so they can be targeted to specific regions and compartments within the cells, while maintaining reasonably small overall dimensions. Compact QD bioconjugates are necessary for developing intracellular biosensors, such as those based on fluorescence resonance energy transfer (FRET), since this process is highly dependent on the spatial separation between donor and acceptor. With the funding, we are developing a surface-functionalized biocompatible and highly luminescent QDs, conjugate them to target proteins and use these new QD bioconjugates to develop sensing assemblies of protein dynamics and protein activation in live cells. In the present research effort we focus on monitoring microtubule (MT)-end tracking protein EB1 and small GTPase Cdc42, two major regulators of cytoskeleton dynamics.

### **B. Results**

#### **B.1. Morphology and viability of cells injected with EB1 protein-conjugated QDs.**

We studied the feasibility of QD microinjection in living cells and tested for cell viability at different time post-injection. Microinjection circumvents the endocytic pathway and subsequent directed motion paused by passive QD engulfment by the cell. Fig. 1 shows that we can microinject DHLA-capped QDs in the cytoplasm of living Swiss 3T3 fibroblasts. We verified that the cells recovered from the trauma of injection as rapidly as

for mock injection of injection buffer. However, DHLA-capped QDs aggregated relatively rapidly (within ~60 min). Aggregation also occurred with commercially available QDs (Evident and Quantum Dot) (data not shown).

To address this issue, we first noted that DHLA QDs coated with maltose binding protein (MBP) did not aggregate in the cytoplasm of Swiss 3T3 fibroblasts for at least 24 h post-injection (data not shown).

We further showed that QDs conjugated with our protein of interest EB1 did not aggregate. The protein EB1 “tracks” the plus end of growing microtubules. We purified His-tag human EB1 proteins and allowed them to bind DHLA-capped QDs through metal-His coordination. After injection in Swiss 3T3 fibroblasts of QD-EB1 conjugates, we found that EB1 had the same stabilizing effect as MBP: once coordinated to DHLA-capped QDs, the protein EB1 abrogated the aggregation of these QDs for at least 24 h. This is sufficient observation time as all proposed experiments will be conducted within 1-h post-injection. Moreover, as in the case of unconjugated DHLA-capped QDs, we found that mock microinjection (not shown) and microinjection with QD-EB1 conjugates caused neither significant morphological changes of the cell (Fig. 5-1) nor cell apoptosis (as tested by tripan blue assay). The functionalization of the DHLA-capped QDs with the protein EB1 had the important benefit of stabilizing the QDs while leaving the cell mostly intact.

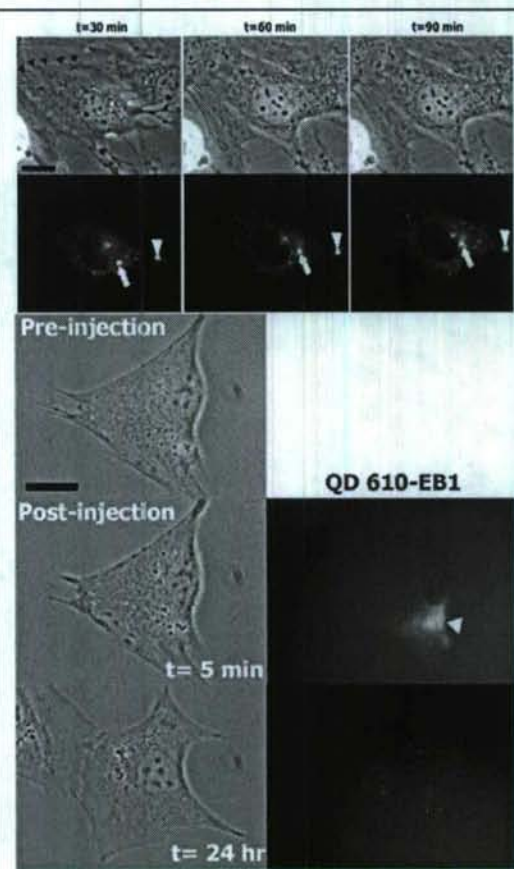


**Fig. 5-1:** (top) Subcellular distribution of un-conjugated and EB1-conjugated DHLA-capped QDs. (A) Overlay of phase-contrast Swiss 3T3 fibroblast and fluorescent bioconjugates after injection of unconjugated DHLA-coated QDs (no conjugated proteins). Arrowheads indicate initial retraction of lamella 30 minutes after injection. The retraction recovers within 60 min, the site of injection becomes reincorporated as shown by movement of the arrow while the arrowhead remains stationary. (bottom) Injection of Swiss 3T3 fibroblasts with QD610-EB1 bioconjugates. Arrowhead indicates point of injection. Cell visualized 5 min and 24 hr after injection of QD-EB1 bioconjugates. Fibroblasts remained viable and exhibited uniform distribution of QDs in cytoplasm. All bars, 20  $\mu$ m.

## B.2. Test of functionality of EB1-conjugated QDs in live cells.

Armed with EB1 QD bioconjugates that preserve cell viability and cell morphology, we verified that the tethering of His EB1 to DHLA-capped QDs retained EB1’s function. EB1 undergoes directed motion from the peri-nucleus region towards the cell periphery through its dynamic binding to the plus end of growing MTs. Our functional assay consists in injecting DHLA-capped QD-EB1 conjugates into Swiss 3T3 fibroblasts and

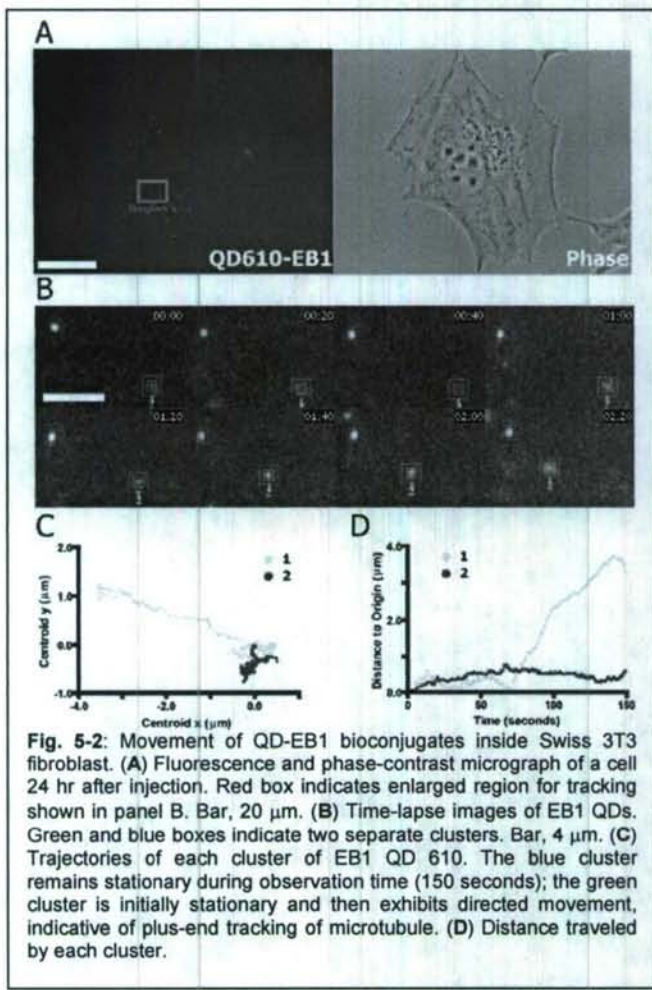


**Fig. 5-2:** Movement of QD-EB1 bioconjugates inside Swiss 3T3 fibroblast. (A) Fluorescence and phase-contrast micrograph of a cell 24 hr after injection. Red box indicates enlarged region for tracking shown in panel B. Bar, 20  $\mu$ m. (B) Time-lapse images of EB1 QDs. Green and blue boxes indicate two separate clusters. Bar, 4  $\mu$ m. (C) Trajectories of each cluster of EB1 QD 610. The blue cluster remains stationary during observation time (150 seconds); the green cluster is initially stationary and then exhibits directed movement, indicative of plus-end tracking of microtubule. (D) Distance traveled by each cluster.

monitor the dynamics of these conjugates using fast image acquisition optics to take advantage of the low photobleaching rate of QDs compared to green fluorescence protein (EGFP). We collected 150 second-long movies at 10 frames/second and tracked the centroid displacements of the QDs using a particle-tracking software as described (Lee et al. 2005). We observed both stationary and highly motile QD-EB1 conjugates (Fig. 5-2). These motile QD-EB1 conjugates underwent directed motion in cytoplasm, from the perinuclear region towards the cell periphery. Control QDs without EB1 were only stationary; application of nocodazole eliminated all motile QD-EB1 conjugates. These results show the preserved functionality of EB1 in live cells and demonstrate the use of QD-EB1 conjugates as efficient markers of plus-end MT dynamics. These results are important as they confirm and exploit the promise of

QD-protein conjugates to allow high frame rate imaging and long exposition times, due mainly to their much higher photobleaching threshold compared to fluorescent proteins. These experiments, though preliminary, demonstrate the use of QD-protein conjugates for monitoring the dynamics of cytoplasmic proteins as opposed to membrane-bound proteins.

## REFERENCES

Amann KJ, Pollard TD. 2001. Direct real-time observation of actin filament branching mediated by Arp2/3 complex using total internal reflection fluorescence microscopy. *Proc Natl Acad Sci U S A* 98(26):15009-13.

Bernheim-Groszasser A, Wiesner S, Golsteyn RM, Carlier MF, Sykes C. 2002. The dynamics of actin-based motility depend on surface parameters. *Nature* 417(6886):308-11.

Dickinson RB, Purich DL. 2006. Diffusion rate limitations in actin-based propulsion of hard and deformable particles. *Biophys J* 91(4):1548-63.

Harbeck B, Huttelmaier S, Schluter K, Jockusch BM, Illenberger S. 2000. Phosphorylation of the vasodilator-stimulated phosphoprotein regulates its interaction with actin. *J Biol Chem* 275(40):30817-25.

Horstrup K, Jablonka B, Honig-Liedl P, Just M, Kochsiek K, Walter U. 1994. Phosphorylation of focal adhesion vasodilator-stimulated phosphoprotein at Ser157 in intact human platelets correlates with fibrinogen receptor inhibition. *Eur J Biochem* 225(1):21-7.

Interliggi KA, Zeile WL, Hens S, McGuire GE, Purich DL, Dickinson RB. 2007. Guidance of actin filament elongation on filament-binding tracks. *Langmuir* In press.

Kuhn JR, Pollard TD. 2005. Real-time measurements of actin filament polymerization by total internal reflection fluorescence microscopy. *Biophys J* 88(2):1387-402.

Lambrechts A, Kwiatkowski AV, Lanier LM, Bear JE, Vandekerckhove J, Ampe C, Gertler FB. 2000. cAMP-dependent protein kinase phosphorylation of EVL, a Mena/VASP relative, regulates its interaction with actin and SH3 domains. *J Biol Chem* 275(46):36143-51.

Laurent V, Loisel TP, Harbeck B, Wehman A, Grobe L, Jockusch BM, Wehland J, Gertler FB, Carlier MF. 1999. Role of proteins of the Ena/VASP family in actin-based motility of *Listeria monocytogenes*. *J Cell Biol* 144(6):1245-58.

Lee JS, Chang MI, Tseng Y, Wirtz D. 2005. Cdc42 mediates nucleus movement and MTOC polarization in Swiss 3T3 fibroblasts under mechanical shear stress. *Mol Biol Cell* 16(2):871-80.

Sturm C. 2007. Analysis of Actin Filament Polymerization on Biomimetic Particles [PhD]. Gainesville: FL.

Svitkina TM, Borisy GG. 1999. Arp2/3 complex and actin depolymerizing factor/cofilin in dendritic organization and treadmilling of actin filament array in lamellipodia. *J Cell Biol* 145(5):1009-26.

Welch MD, Mitchison TJ. 1998. Purification and assay of the platelet Arp2/3 complex. *Methods Enzymol* 298:52-61.

Wiesner S, Helfer E, Didry D, Ducouret G, Lafuma F, Carlier MF, Pantaloni D. 2003. A biomimetic motility assay provides insight into the mechanism of actin-based motility. *J Cell Biol* 160(3):387-98.

Yarar D, To W, Abo A, Welch MD. 1999. The Wiskott-Aldrich syndrome protein directs actin-based motility by stimulating actin nucleation with the Arp2/3 complex. *Curr Biol* 9(10):555-8.

Zeile WL, Zhang F, Dickinson RB, Purich DL. 2005. Listeria's right-handed helical rocket-tail trajectories: mechanistic implications for force generation in actin-based motility. *Cell Motil Cytoskeleton* 60(2):121-8.

**Personnel Supported:****UF:**

Richard B. Dickinson (PI)  
Daniel Purich (co-PI)  
William Zeile (research scientist)  
Adam Feinberg (postdoc)  
Kimberly Interliggi (graduate student)  
Catherine Marcinkiewcz (graduate student)

**William & Mary:**

Brian Holloway (faculty)  
Bill Cooke (faculty)  
Michael Trosset (faculty)  
Benjamin French (post-doc)  
Haijian Chen (post-doc)  
Christine Bunai (Research Scientist)  
Christine Hopkins (graduate student)

**Associated:**

Gene Tracy (faculty)

**International Technologies Center:**

Gary McGuire: (Sub-award PI)  
Suzanne Hens (Scientist)  
Mark Ray (Scientist)  
Darin Thomas (Scientist)

**Johns Hopkins University:**

Denis Wirtz (Sub-award PI)  
Melissa Thomson (graduate student)

**Publications:**

Interliggi, K. A., Zeile, W. L. Hens, S., McGuire, G. E., Purich, D. L. and R. B. Dickinson. "Guidance of Actin Filament Elongation on Filament-Binding Tracks". *Langmuir* 2007. In Press.

Dickinson, R. B. and D. L. Purich. "Nematode Sperm Motility: Non-Polar Filament Polymerization Mediated by End-Tracking Motors" *Biophysical Journal* 15;92(2):622-31 (2007).

Sturm, C. ANALYSIS OF ACTIN FILAMENT POLYMERIZATION ON BIOMIMETIC PARTICLES.  
PhD Thesis, University of Florida, 2007

Dickinson. R. B. and D. L. Purich. "Diffusion rate limitations in actin-based propulsion of hard and deformable particles" *Biophysical Journal* 91(4):1548-63 (2006)

### **Interactions/Transitions:**

#### **a. Participation/presentations at meetings, conferences, seminars, etc.**

"Models for Cell Motility by Filament Elongation Motors" Plenary Lecture to at the International Congress of Industrial and Applied Mathematics. Zurich, Switzerland. July 17, 2007.

"Shared Fiber-Growth Mechanisms of Particle-Catalyzed Carbon Nanofiber Synthesis and Actin "Rocket Tails" Formed during Actin-Based Propulsion of Intracellular Particles." R. Dickinson. 17<sup>th</sup> US Army Symposium on Solid Mechanics, Baltimore, MD. April 5, 2007. Paper J9

(Invited) "Clever Bugs: Microbial Hijacking of the Host Cell Adhesion and Motility Systems", R. Dickinson. AICHE Annual Meeting, San Francisco, CA. Nov. 2006. Paper 131e.

"Characterization of Actin-Based Motility on Patterned Substrata", Kimberly A. Interliggi, William Zeile, Suzanne Ciftan Hens, Gary McGuire, Daniel L. Purich, and Richard B. Dickinson. AICHE Annual Meeting, San Francisco, CA. Nov. 2006. Paper 112f.

"A Model for Force Generation by Microtubule End-Binding Proteins", L. Caro, R Dickinson, and D. L. Purich. AICHE Annual Meeting, San Francisco, CA. Nov. 2006. Paper 338c

(Invited) "A Model for Force Generation by the Microtubule End-Binding Protein EB1", L. Caro, R. Dickinson, and D. L. Purich. *Molecular Motors* Session. BMES Annual Meeting, Chicago, IL. Oct. 2006.

"Directionally Guided Actin-Based Particle Motility in Vitro". K. Interliggi, A. Feinberg, W. Zeile, S. Hens, G. McGuire, D. L. Purich, and R. B. Dickinson. AICHE Annual Meeting. Cincinnati, OH. Nov. 2005. Paper 578e.

(Invited) "Mechanical Properties of Force Production by Filament End-Tracking Motors". R. Dickinson and D. Purich Platform Session: Assembly and Mechanics of the Cytoskeleton. BMES Annual Meeting, Baltimore, MD., Sept. 29, 2005. Paper 437.

"Direct Measurement of Colloidal Forces that Influence Interactions of Calcium Phosphate with a Phospholipid Bilayer" J. Sharp and R. Dickinson. International Symposium on the Role of Adsorbed Films and Particulate Systems in Nano and Biotechnologies, Gainesville, FL August 24-26, 2005. Session 1.5:

"Force Generation by Cytoskeletal Filament End-Tracking Proteins", R. Dickinson and D. Purich. Biophysical Society Meeting, Platform Session E: Actin and Actin-Binding Proteins, Long Beach, CA, Feb. 13 2005.

"Diffusion-Limitations in Actin-Based Motility", R. Dickinson and D. Purich, AICHE Annual Meeting, , Austin, TX November 2004

"Force Generation by Cytoskeletal Filament End-Tracking Proteins" R. Dickinson, L. Caro, and D. Purich. AICHE Annual Meeting, Austin, TX. November 2004

(Invited) "Actin-Based Motility in Biomimetic Systems: Diffusion-Limited Elongation of Tethered Filaments", R. Dickinson and D Purich. BMES Annual Meeting, Philadelphia, PA. October, 2004. Paper 849. Abstract 125286.

Richard Dickinson, Daniel Purich, and Bill Cooke participated in the DARPA Biomolecular Motors meeting in Monterey, CA and in Washington DC.

**b. Consultative and advisory functions**

None.

**c. Transitions.**

Task 3: Collaboration with Incogen, a local bioinformatics company, to use the peak picking software being developed has been started.

**New Discoveries, Inventions, Patent Disclosures:**

Task 3: New peak detection software has been patented as U.S. patent 7,219,038 B2.

**Honors/Awards:**

Dickinson was awarded the University of Florida Research Foundation Professorship (2005).

Dickinson gave a plenary lecture at the International Congress of Industrial and Applied Mathematics. Zurich, Switzerland. July 17, 2007.